Synchrotron Light Sources in Modern Science and Technology: the example of the Elettra Laboratory

Massimo Altarelli

Abdus Salam International Center for Theoretical Physics, 34100 Trieste (Italy)

Present Adress: *European XFEL Project Team*
c/o DESY
Notkestr. 85, 22607 Hamburg, Germany

Some dates in the history of science...

1895 Discovery of x-rays by Röntgen

1905 Einstein explains the photoelectric effect by Planck's quantum theory

1912 Laue's discovery of x-ray diffraction by crystals

1947 First experimental observation of synchrotron light by R.F. Elder *et al.*

1953 Double-helix structure of DNA elucidated by x-ray diffraction

Radiation from Electrons in a Synchrotron

F. R. ELDER, A. M. GUREWITSCH, R. V. LANGMUIR,
AND H. C. POLLOCK
*Research Laboratory, General Electric Company,
Schenectady, New York*
May 7, 1947

HIGH energy electrons which are subjected to large accelerations normal to their velocity should radiate electromagnetic energy.[1–4] The radiation from electrons in a betatron or synchrotron should be emitted in a narrow cone tangent to the electron orbit, and its spectrum should extend into the visible region. This radiation has now been observed visually in the General Electric 70-Mev synchrotron.[5] This machine has an electron orbit radius of 29.3 cm and a peak magnetic field of 8100 gausses. The radiation is seen as a small spot of brilliant white light by an observer looking into the vacuum tube tangent to the orbit

Beamline

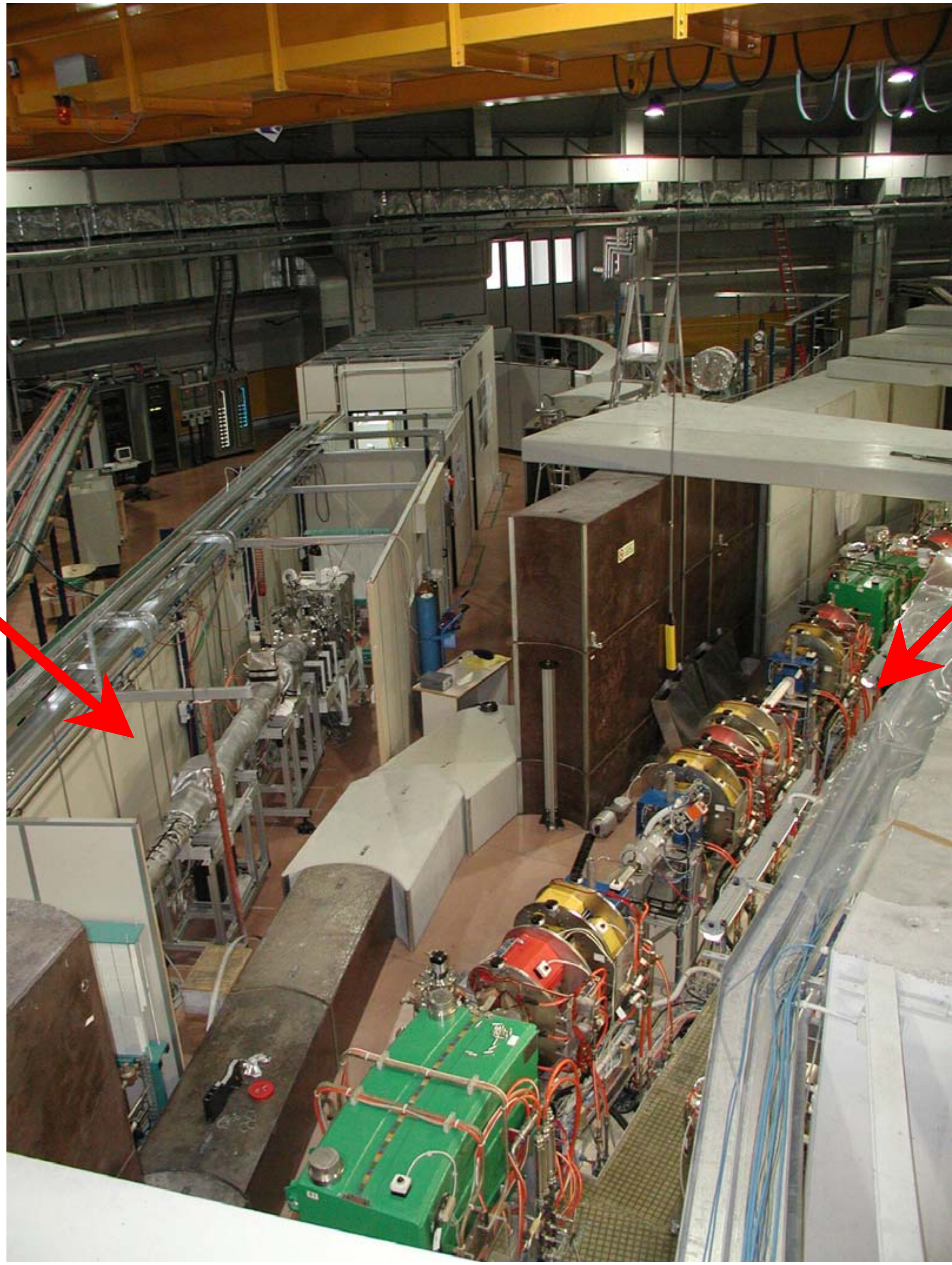

Storage Ring

QuickTime™ and a
TIFF (Uncompressed) decompressor
are needed to see this picture.

What is a Synchrotron Light Source ?

A synchrotron is a large machine (about the size of a football field) that accelerates electrons to almost the speed of light. As the electrons are deflected through magnetic fields they create extremely bright light. The light is channelled down beamlines to experimental stations where it is used for research.

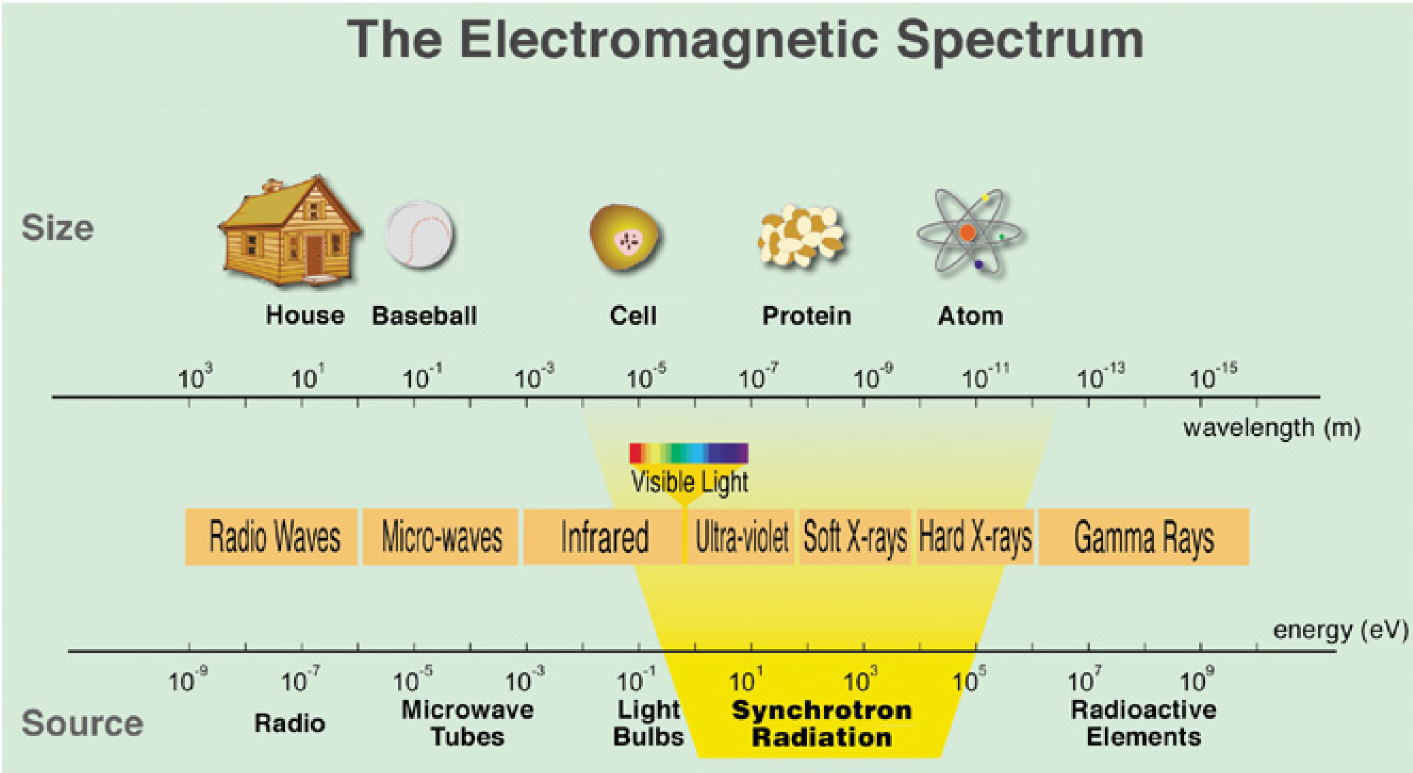

The Electromagnetic Spectrum
Size
House
Baseball
Cell
Protein
Atom
10^3 10^1 10^-1 10^-3 10^-5 10^-7 10^-9 10^-11 10^-13 10^-15
wavelength (m)
Visible Light
Radio Waves
Micro-waves
Infrared
Ultra-violet
Soft X-rays
Hard X-rays
Gamma Rays
energy (eV)
10^-9 10^-7 10^-5 10^-3 10^-1 10^1 10^3 10^5 10^7 10^9
Source
Radio
Microwave Tubes
Light Bulbs
Synchrotron Radiation
Radioactive Elements

SYNCHROTRON LIGHT : VERY BRIGHT EMISSION OF ELECTROMAGNETIC RADIATION FROM ELECTRONS ORBITING IN A STORAGE RING.

IT IS THE BRIGHTEST AVAILABLE SOURCE OF ULTRAVIOLET AND X-RAY RADIATION USED FOR RESEARCH IN :

- -CONDENSED MATTER AND MATERIALS PHYSICS
- -SURFACE AND INTERFACE PHYSICS AND CHEMISTRY
- -STRUCTURAL BIOLOGY (30% OF WORLDWIDE USE)
- -IMAGING (METALLURGY, MATERIALS SCIENCE, MEDICINE)
- -MICROFABRICATION

THERE ARE ABOUT 45 DEDICATED SOURCES WORLDWIDE, 10 OF THEM BEING OF THE MOST ADVANCED TYPE (INCLUDING ELETTRA IN TRIESTE, ITALY) AND AT LEAST 3 MORE ARE UNDER CONSTRUCTION.

Brilliance / Spectral Brightness

$$\frac{\textbf{FLUX OF PHOTONS IN UNIT SPECTRAL RANGE}}{\textbf{(SOURCE AREA) X (BEAM DIVERGENCE)}}$$

Units: Photons/s/mm^2/mrad^2/0.1% bandwidth

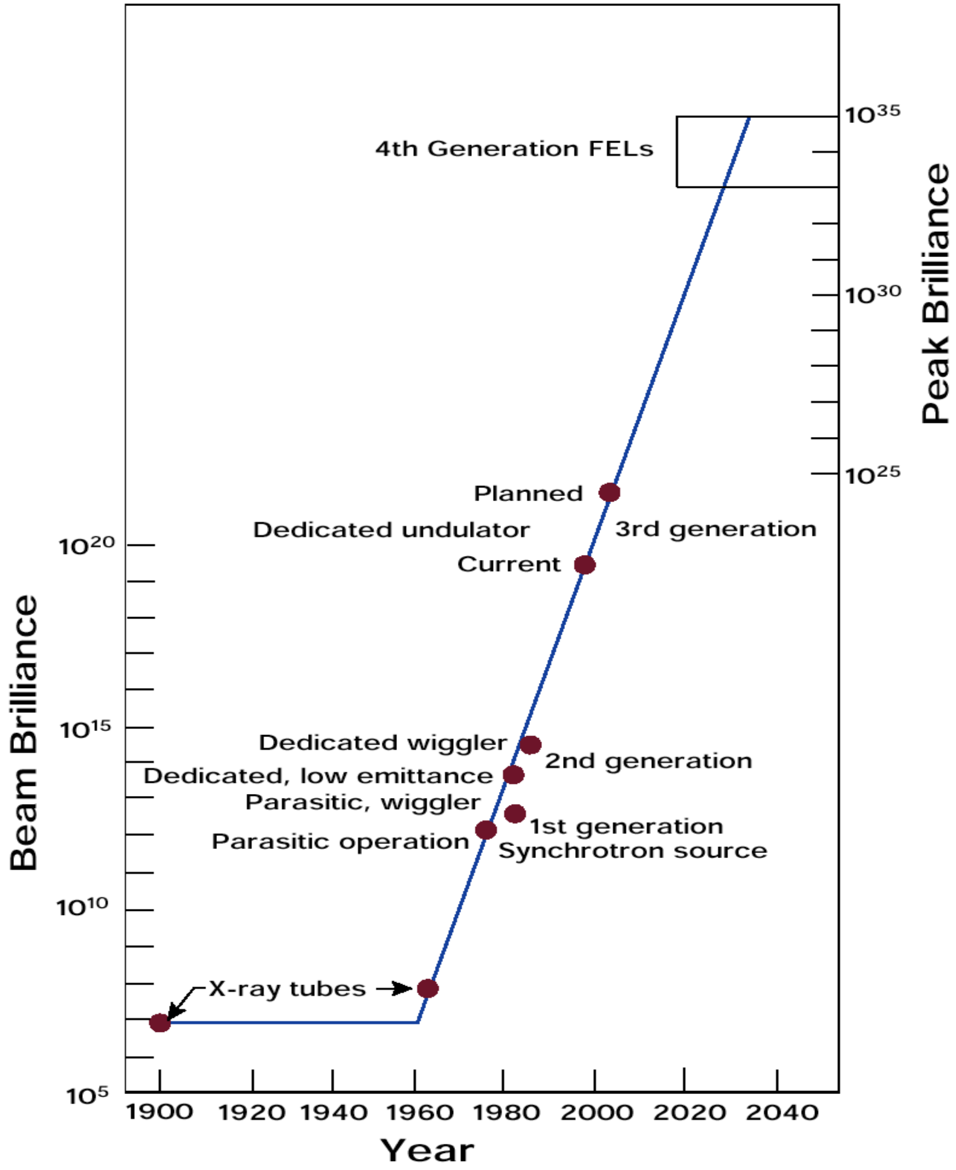

Fig. 1: History of (8-keV) x-ray sources, beam brilliance vs. time.

Synchrotron Light Sources

FIRST GENERATION:
Accelerators and storage rings built for other purposes, parasitically used as light sources

SECOND GENERATION:
Dedicated rings designed and optimised as light sources

THIRD GENERATION:
Dedicated rings built to maximise brilliance by reducing the beam emittance and by the extensive use of undulators as light sources

FOURTH GENERATION:
Diffraction-limited VUV and X-ray sources, with full spatial coherence:
Free electron lasers based on Linacs, Energy-Recovery Linacs.

elettra

Third Generation Synchrotron Light Sources

Low Emittance of Storage Ring

(Emittance = Size of particle beam *X* angular divergence)

“ Insertion Devices” for Synchrotron Light Production

==> High Brilliance (Spectral Brightness)

Evolution of Synchrotron Radiation

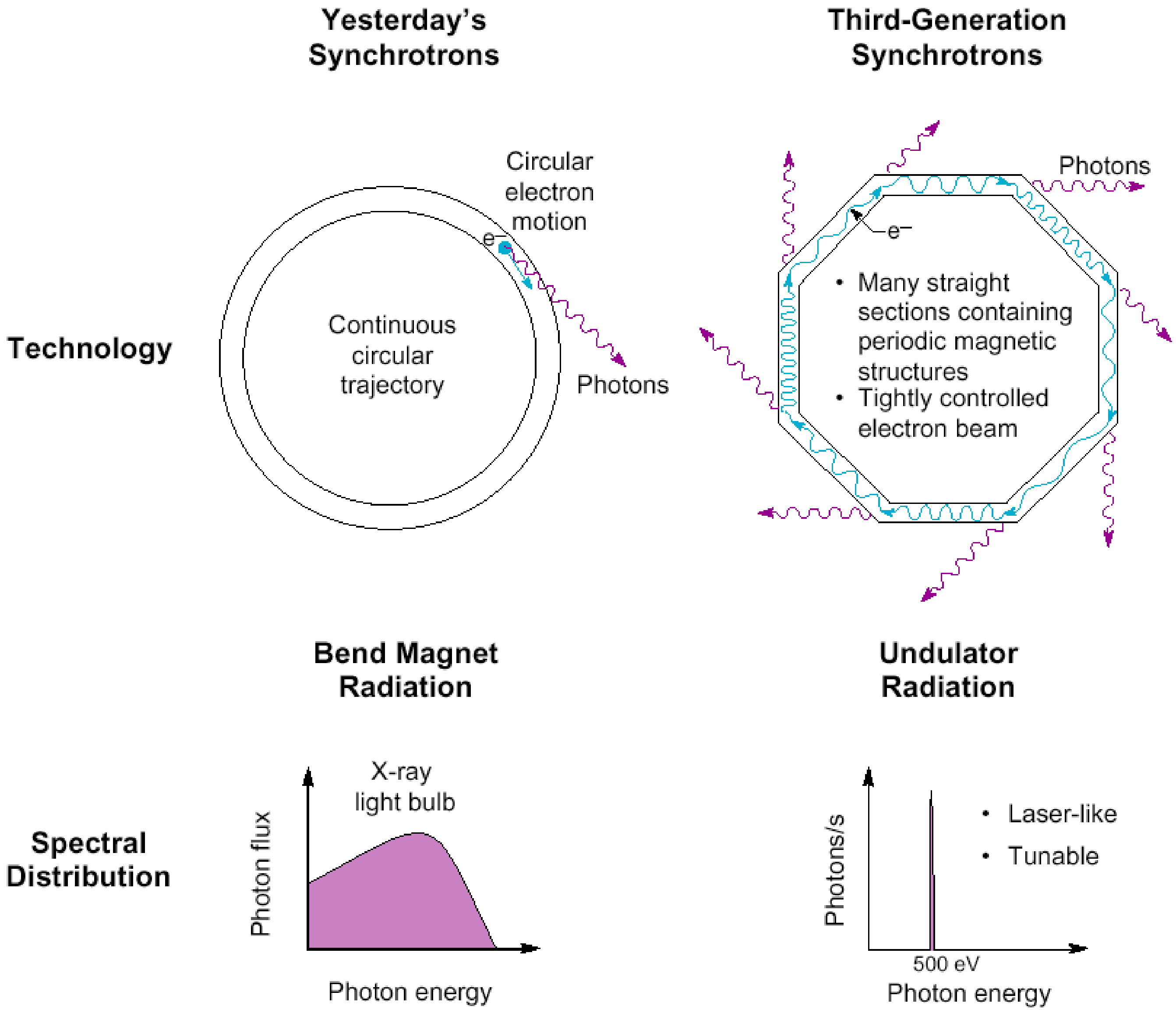

Insertion Devices (Undulators, Wigglers) Principle

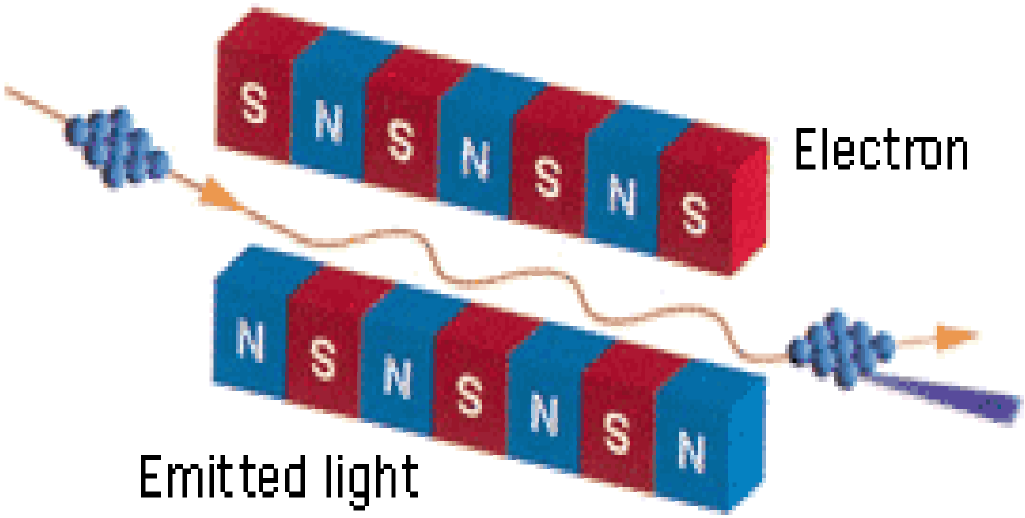

Permanent Magnet Undulator

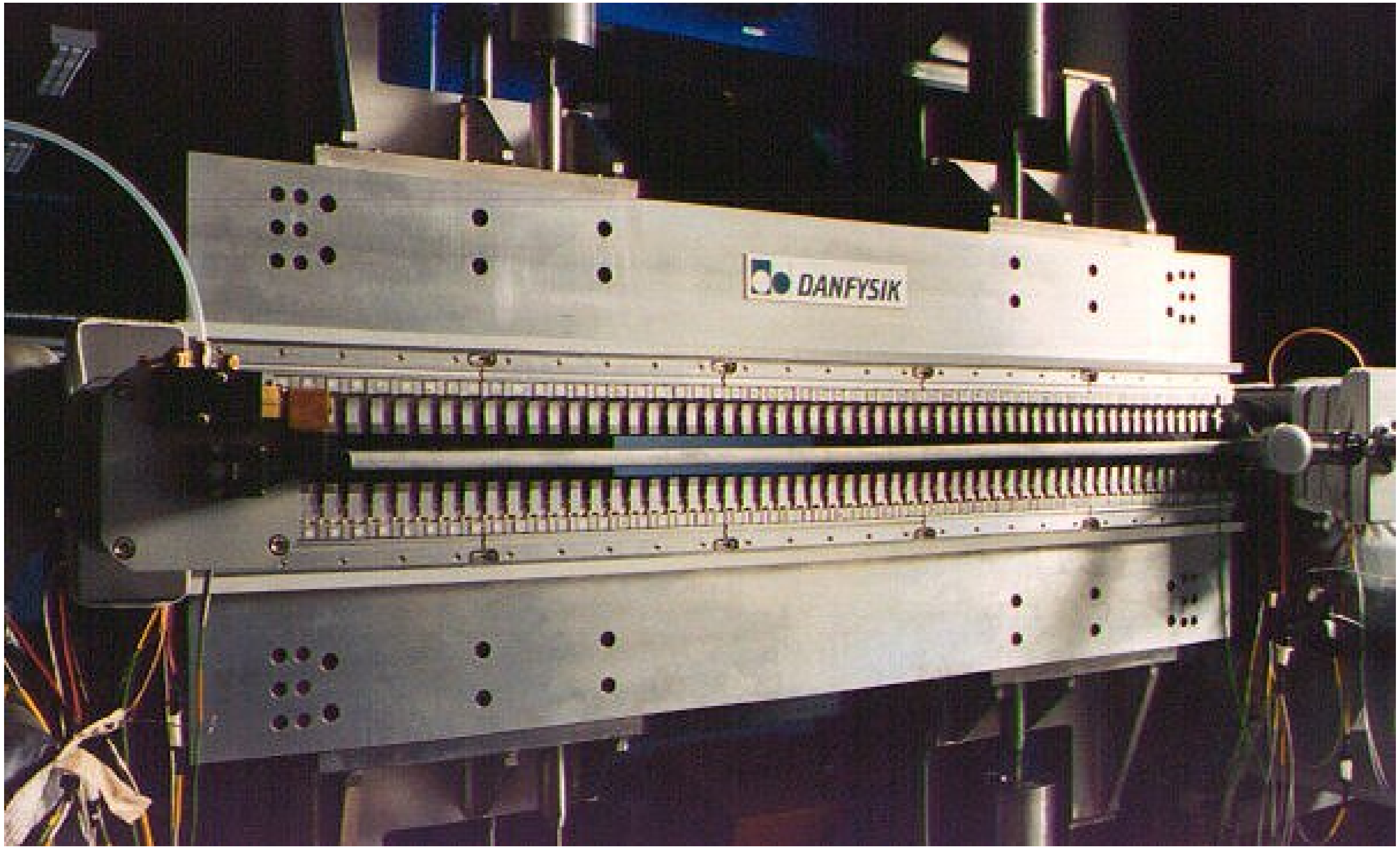

Third Generation Synchrotron Sources

VUV-Soft X Sources
E< 3 GeV

- Elettra (I)
- ALS (USA)
- BESSY II(D)
- Max II (S)
- Swiss Light Source (CH)
- Taiwan SRC
- Pohan Light Source (S. Korea)

Hard X Sources
E> 5 GeV

- ESRF (Europe)
- APS (USA)
- Spring 8 (Japan)

ELETTRA Laboratory

ESRF, Grenoble (France)

Swiss Light Source, Villigen (CH)

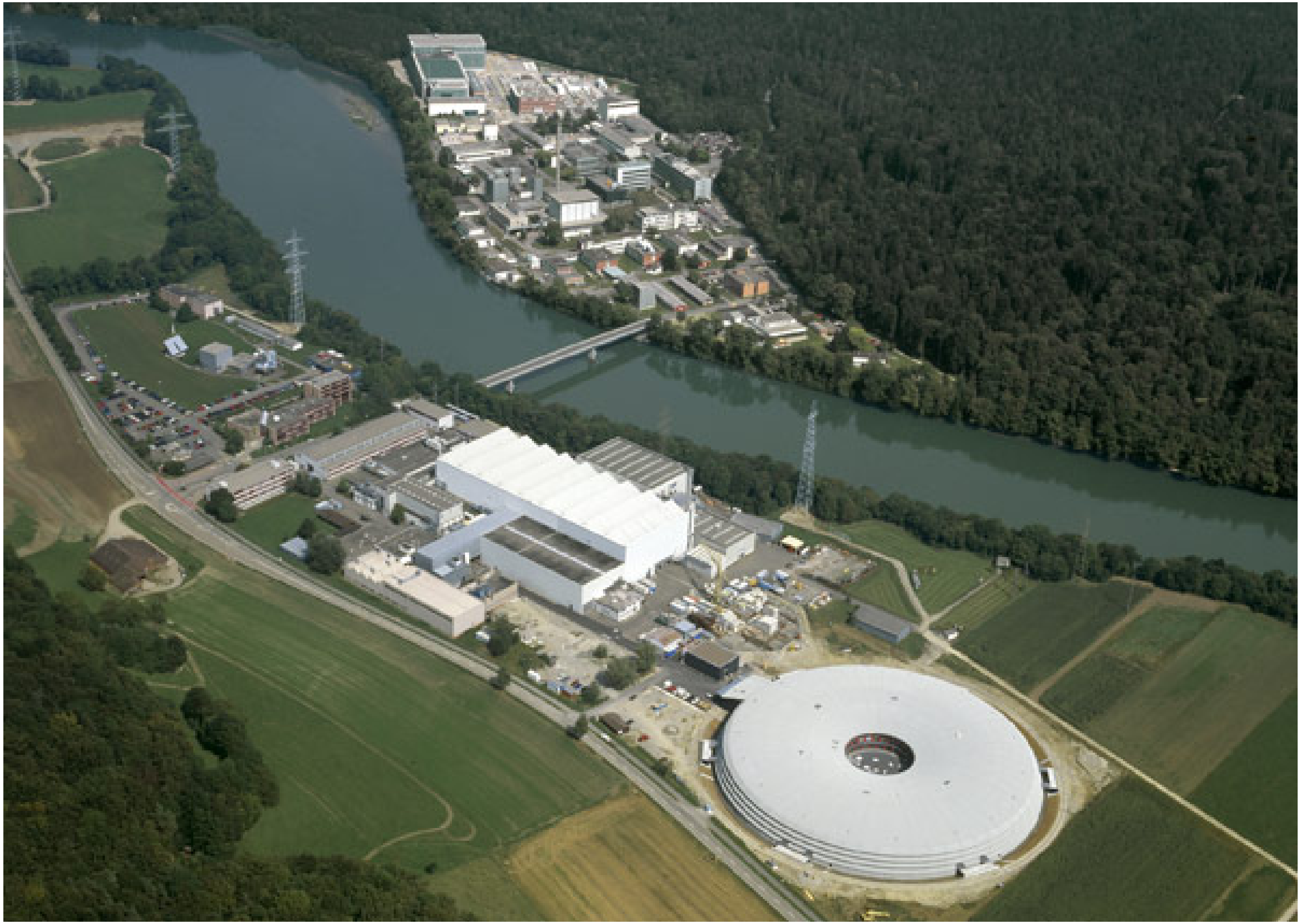

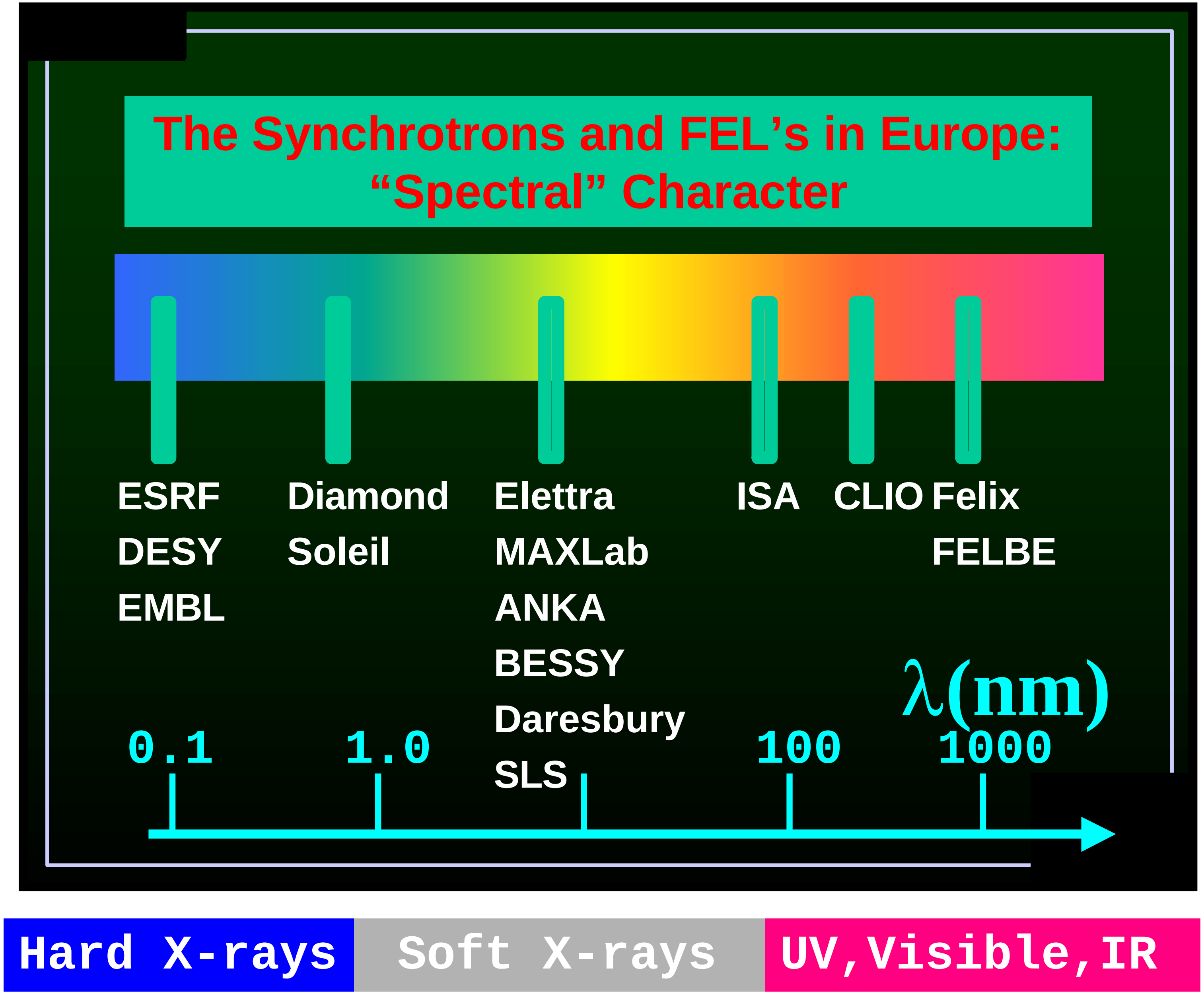

The Synchrotrons and FEL's in Europe:
"Spectral" Character
ESRF
DESY
EMBL
Diamond
Soleil
Elettra
MAXLab
ANKA
BESSY
Daresbury
SLS
ISA
CLIO
Felix
FELBE
λ(nm)
0.1
1.0
100
1000
Hard X-rays
Soft X-rays
UV,Visible,IR

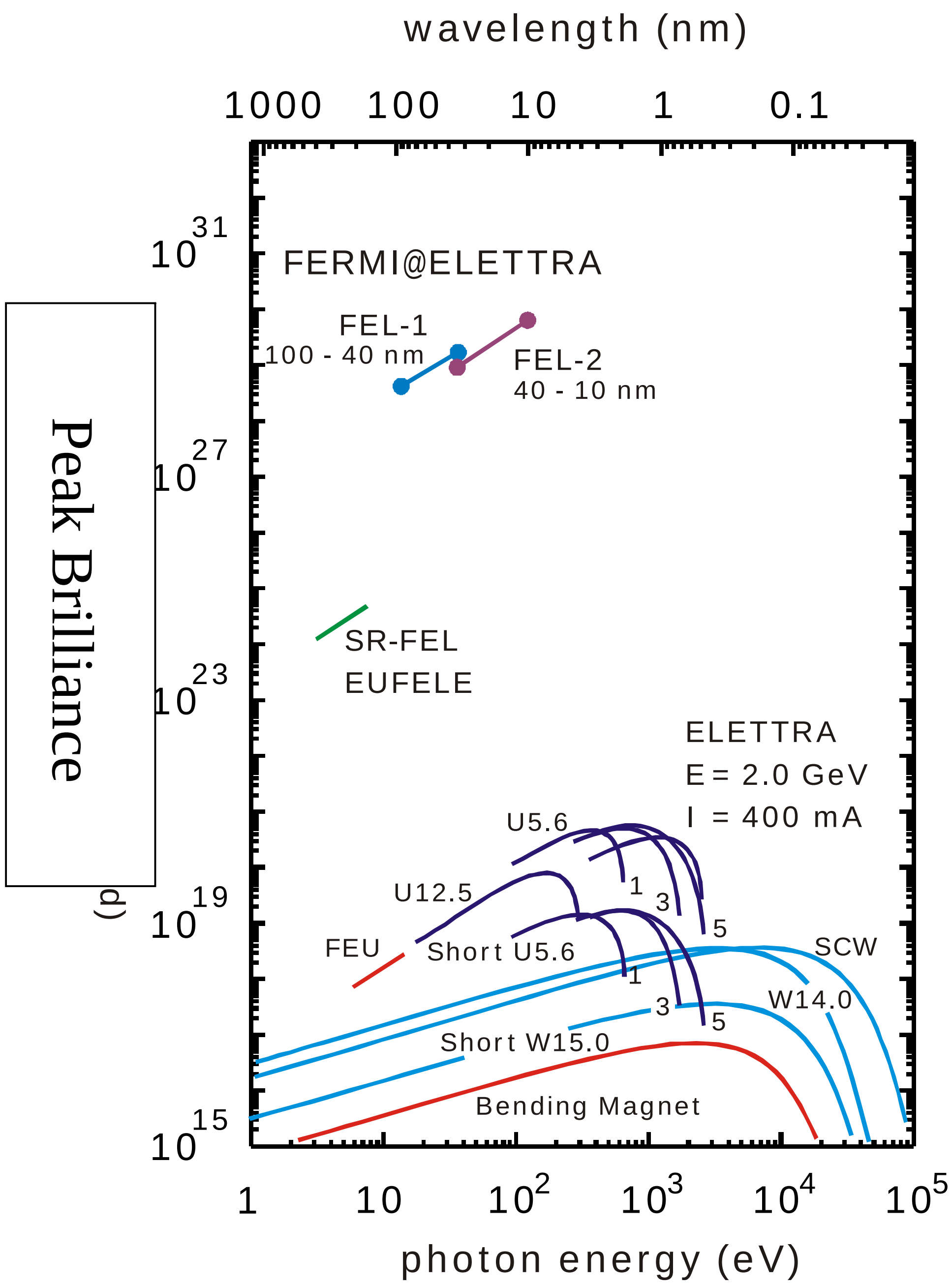

wavelength (nm)
1000
100
10
1
0.1
FERMI@ELETTRA
FEL-1
100 - 40 nm
FEL-2
40 - 10 nm
SR-FEL
EUFELE
ELETTRA
E = 2.0 GeV
I = 400 mA
U5.6
U12.5
FEU
Short U5.6
SCW
W14.0
Short W15.0
Bending Magnet
Peak Brilliance
10^{31}
10^{27}
10^{23}
10^{19}
10^{15}
1
10
10^2
10^3
10^4
10^5
photon energy (eV)

Elettra Beamlines

Elettra Beamlines

19 Fully Operational Beamlines

Elettra Beamlines

19 Fully Operational Beamlines

3 Partly Operational (Commissioning) Beamlines: Infrared

Elettra Beamlines

19 Fully Operational Beamlines

3 Partly Operational (Commissioning) Beamlines: Infrared

Microfluorescence

Elettra Beamlines

19 Fully Operational Beamlines

3 Partly Operational (Commissioning) Beamlines: Infrared

Microfluorescence

Bad-Elph (hi resol. photoem.)

Elettra Beamlines

19 Fully Operational Beamlines

3 Partly Operational (Commissioning) Beamlines: Infrared

Microfluorescence

Bad-Elph (hi resol. photoem.)

1 Storage Ring Free Electron Laser

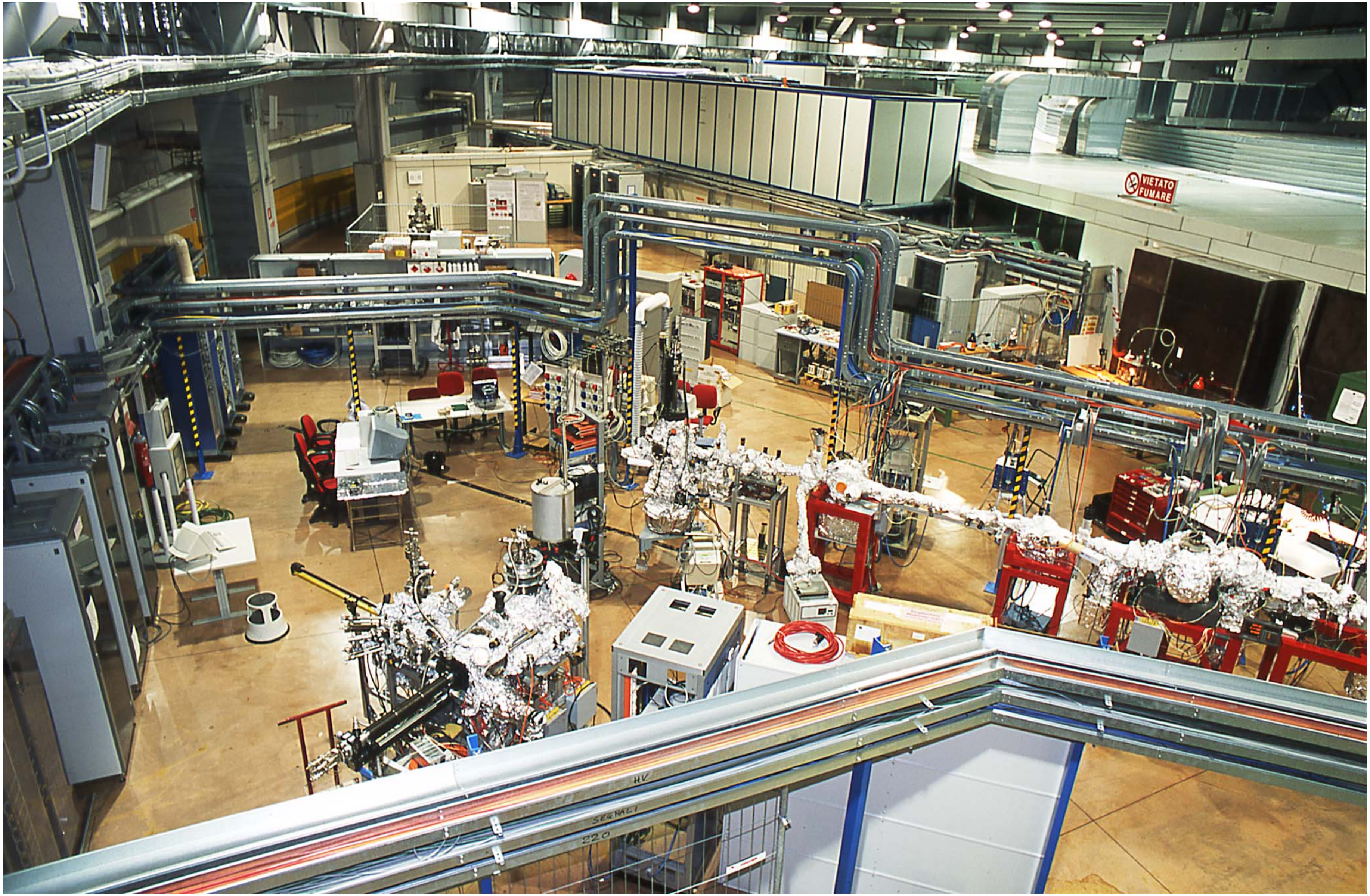
VIETATO
FUMARE
HV
SEGNALI
220

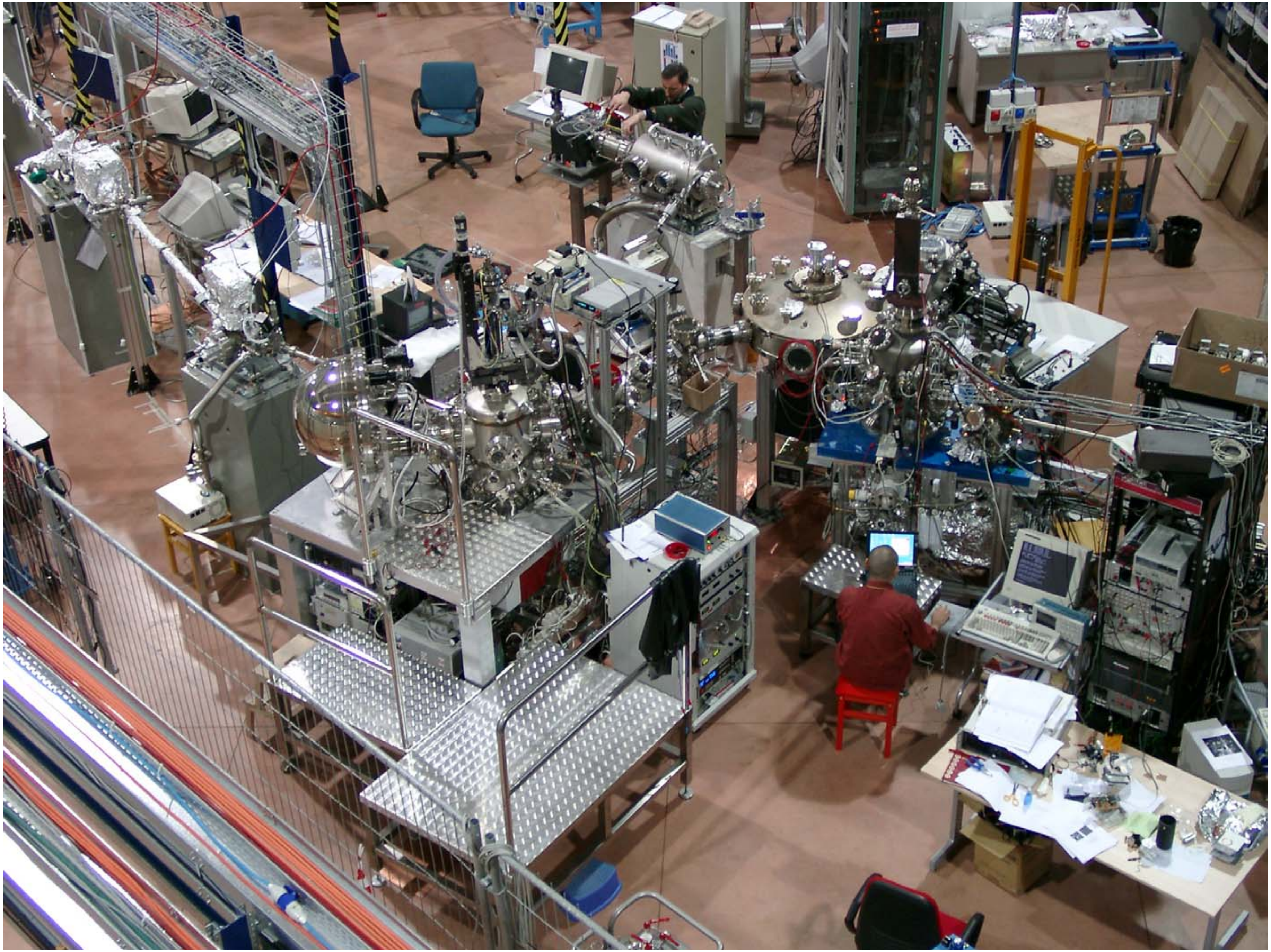

Monochromator + Analyzer

The IUVS Beamline

Available probes to measure the $S(Q,\omega)$

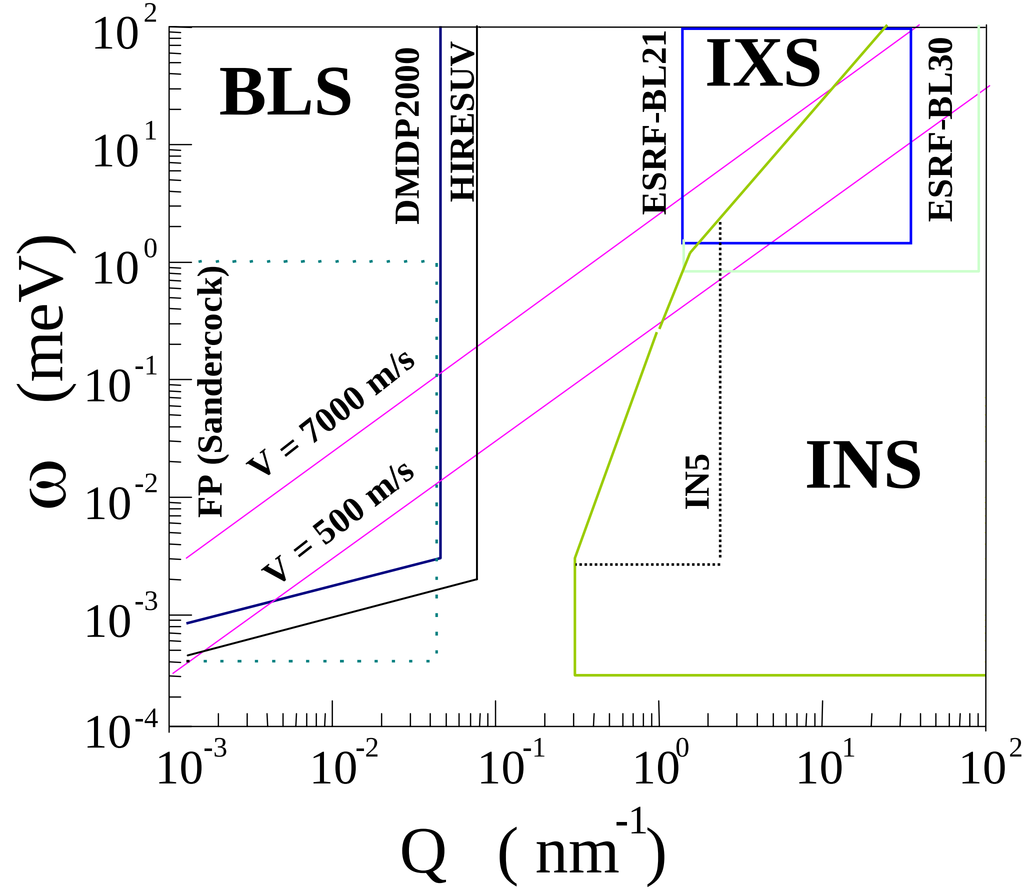

Available probes to measure the S(Q,ω)

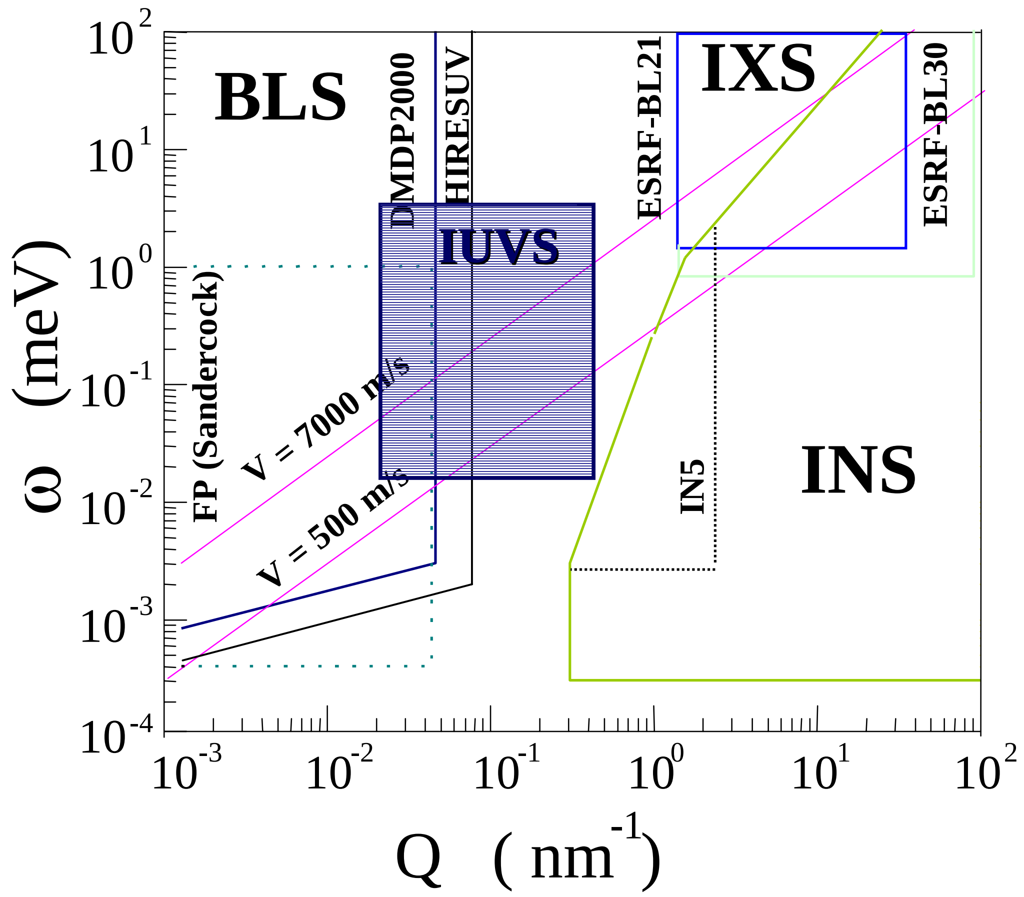

Investigations in the Intermediate Region could Shed Light on:

Liquids - Fluids

- Transition from the Hydrodynamic to the Kinetic regime in Simple liquids and fluids.
- Effect of the Local Structure on the Collective Dynamics in Molecular liquids and H-bonded liquids.
- Liquid Metals

Glasses

- Nature of the Vibrational Modes in the Mesoscopic space-time region.
- Relaxational Processes in Super-Cooled liquids and their relation to the Glass Transition.
- Vibrational and Relaxational Low Temperature Properties of Fragile and Strong glasses.

Resonant Scattering (Tunability)

- Low count-rate experiments.
- Determination of Partial Dynamic Structure Factor.
- Transverse Dynamics of the system.

First results of the Inelastic Ultraviolet Scattering BL

"Structural relaxation in liquid water by inelastic UV scattering"
C. Masciovecchio, S. C. Santucci, A. Gessini, S. Di Fonzo, G. Ruocco, and F. Sette, *PRL **92**, 255507 (2004)*

"Inelastic ultraviolet scattering from high frequency acoustic modes in glasses"
C. Masciovecchio, A. Gessini, S. Di Fonzo, L. Comez, S. C. Santucci, and D. Fioretto, *PRL **92**, 247401 (2004)*

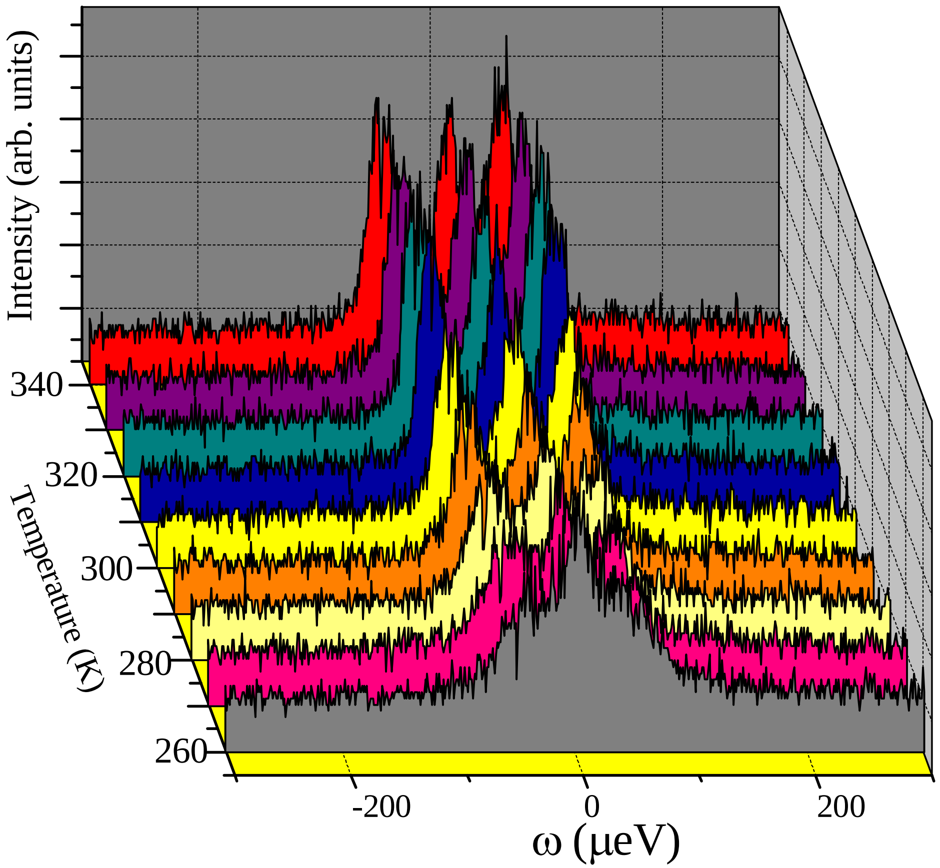

Two single exponential relaxations in memory function of S(Q,ω).

$$S(Q,\omega) = (2C_o^2 q^2/\omega)\mathrm{Im}[\omega^2 - \omega_o^2 - i\omega m_q(\omega)]^{-1}$$

$$m_q(t) = \omega_o^2(\gamma-1)\exp(-D_T q^2 t) + 2\gamma_o\,\delta(t) + (q^2\Delta^2/\rho)\exp(-t/\tau)^{\beta}$$

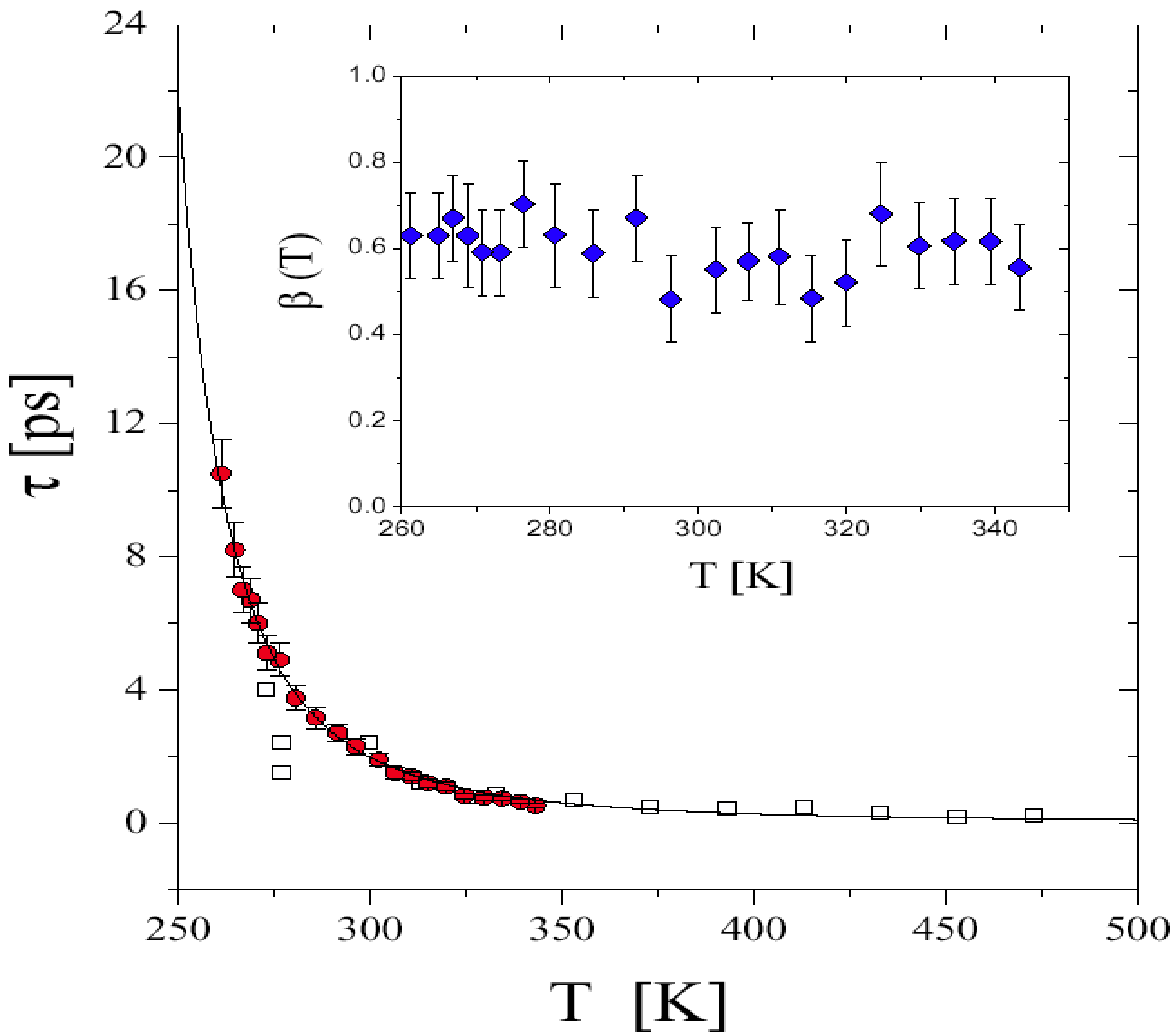

Fig. 1 - Temperature dependence of the structural relaxation time τ of water as obtained by IUVS (red circles). For the sake of comparison Inelastic X-ray Scattering data are also shown (open squares). The solid line represents the Mode Coupling Theory prediction fitted over the displayed experimental points. In the inset we show the temperature dependence of the structural stretching parameter β (blue diamonds). MCT predicts β<1 and temperature independent.

Vitreous Silica

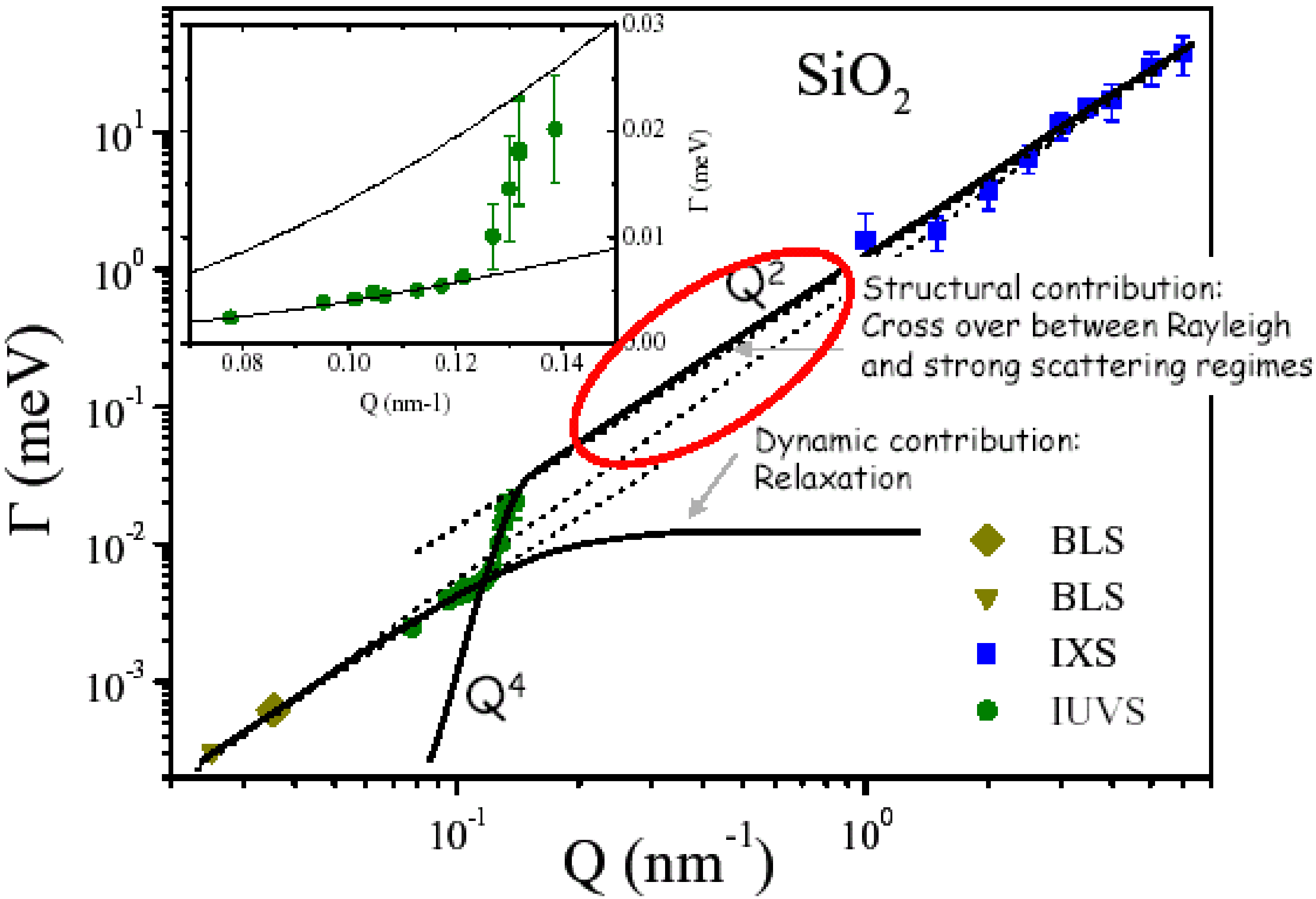

SYRMEP Beamline

Phase Contrast Imaging of

Archeological Glasses

Contrast-formation

- Contrast by Absorption
  - Thickness or density of specimens
  - Absorption from element
  - * Low resolution (> 1mm)
  - * Weak contrast for tissue

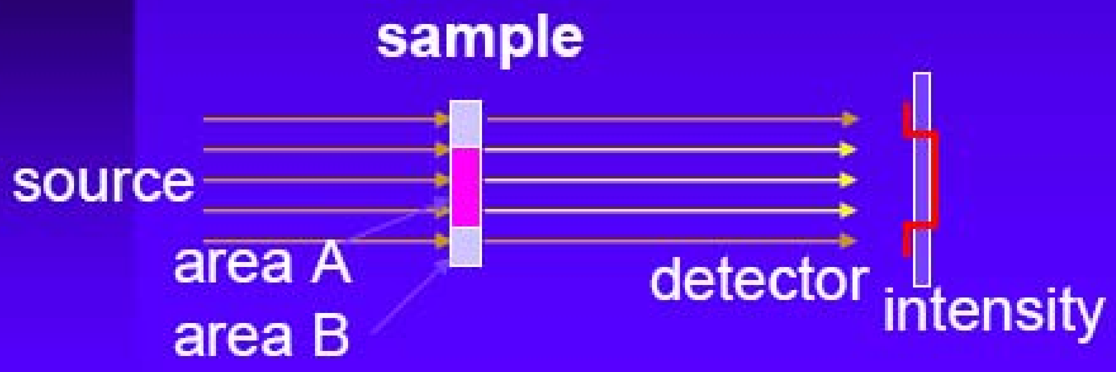

Fresnel diffraction or refraction

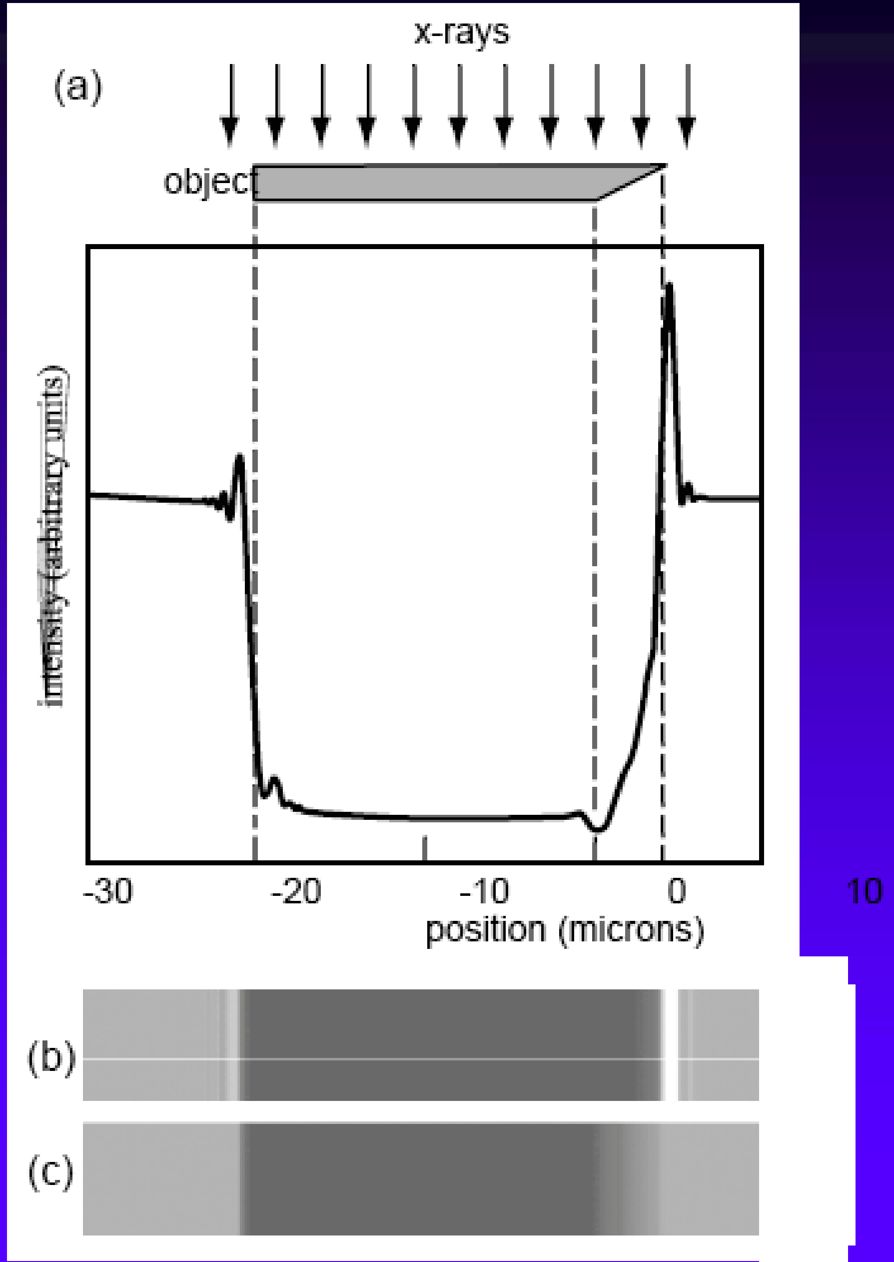

Original waterlogged glass, completely corroded

Fragment provided by the Museum of London

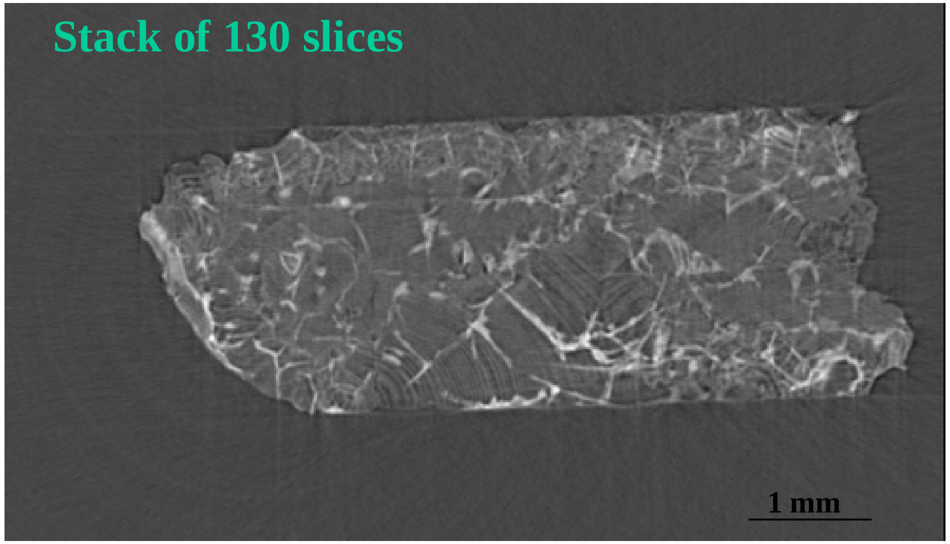

E = 25 keV *d* = 66 cm; *acquisition time: 4h*

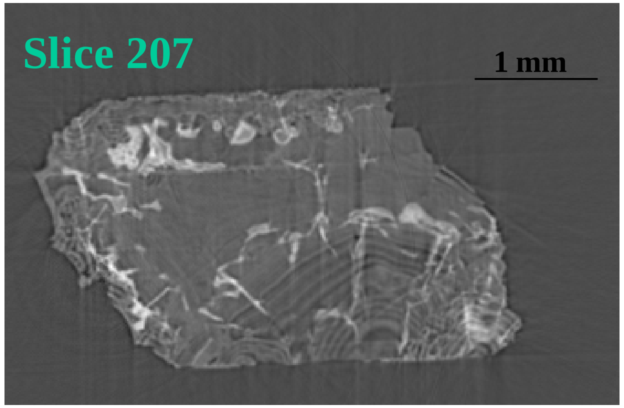

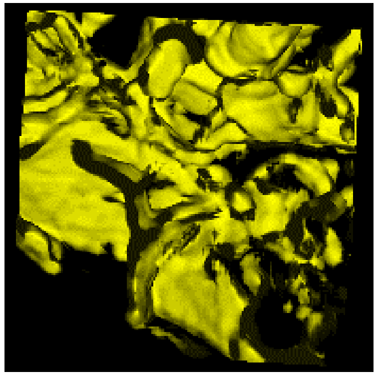

Cine rendering of channels
(9.0 x 9.0 x 0.2) mm^3

Original waterlogged glass, completely corroded

Fragment provided by the Museum of London

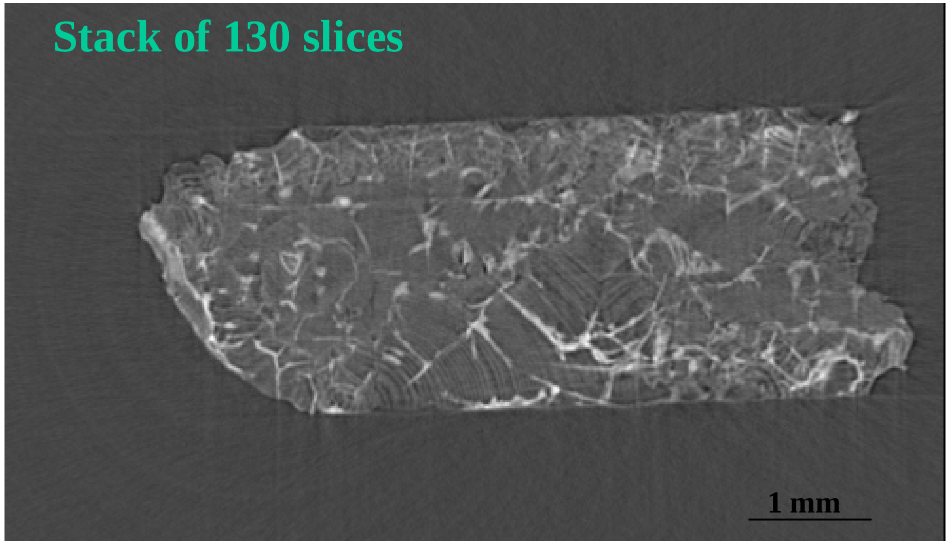

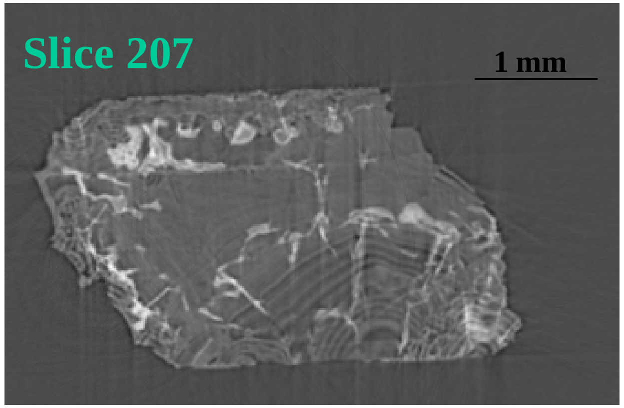

E = 25 keV ***d* = 66 cm;** ***acquisition time: 4h***

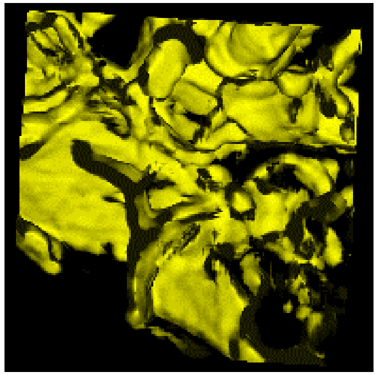

Cine rendering of channels
(9.0 x 9.0 x 0.2) mm^3

It is possible to visualize:

→ the gel-layer channels

→ the lamellar structure inside the corroded glass

QuickTime™ and a
decompressor
are needed to see this picture.

QuickTime™ and a
decompressor
are needed to see this picture.

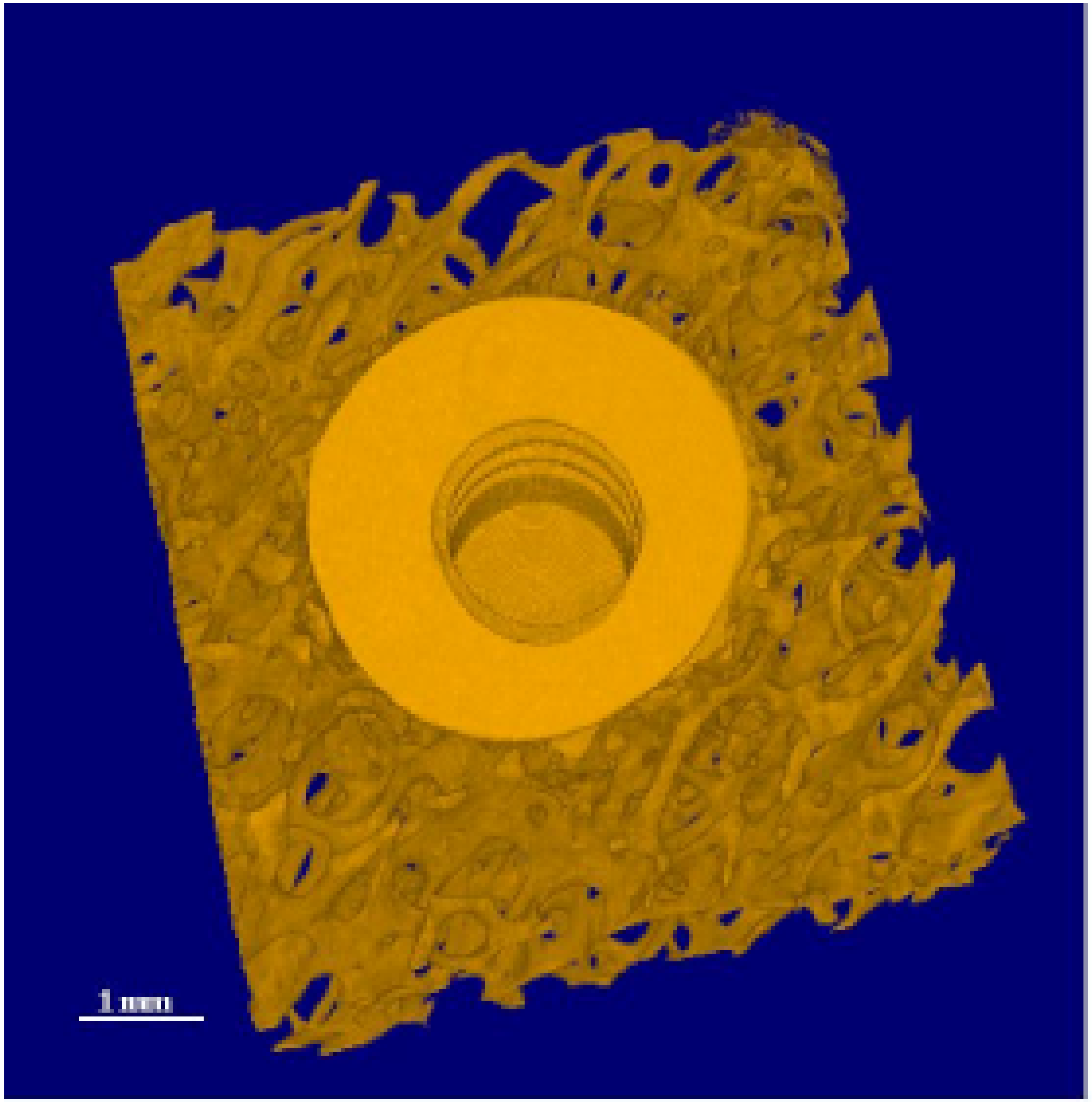

Fig. 2) Example of 3D volume rendering of
an implanted bone. (Courtesy L. Tesei)

Elettra-U. of Trieste

SYRMEP beamline

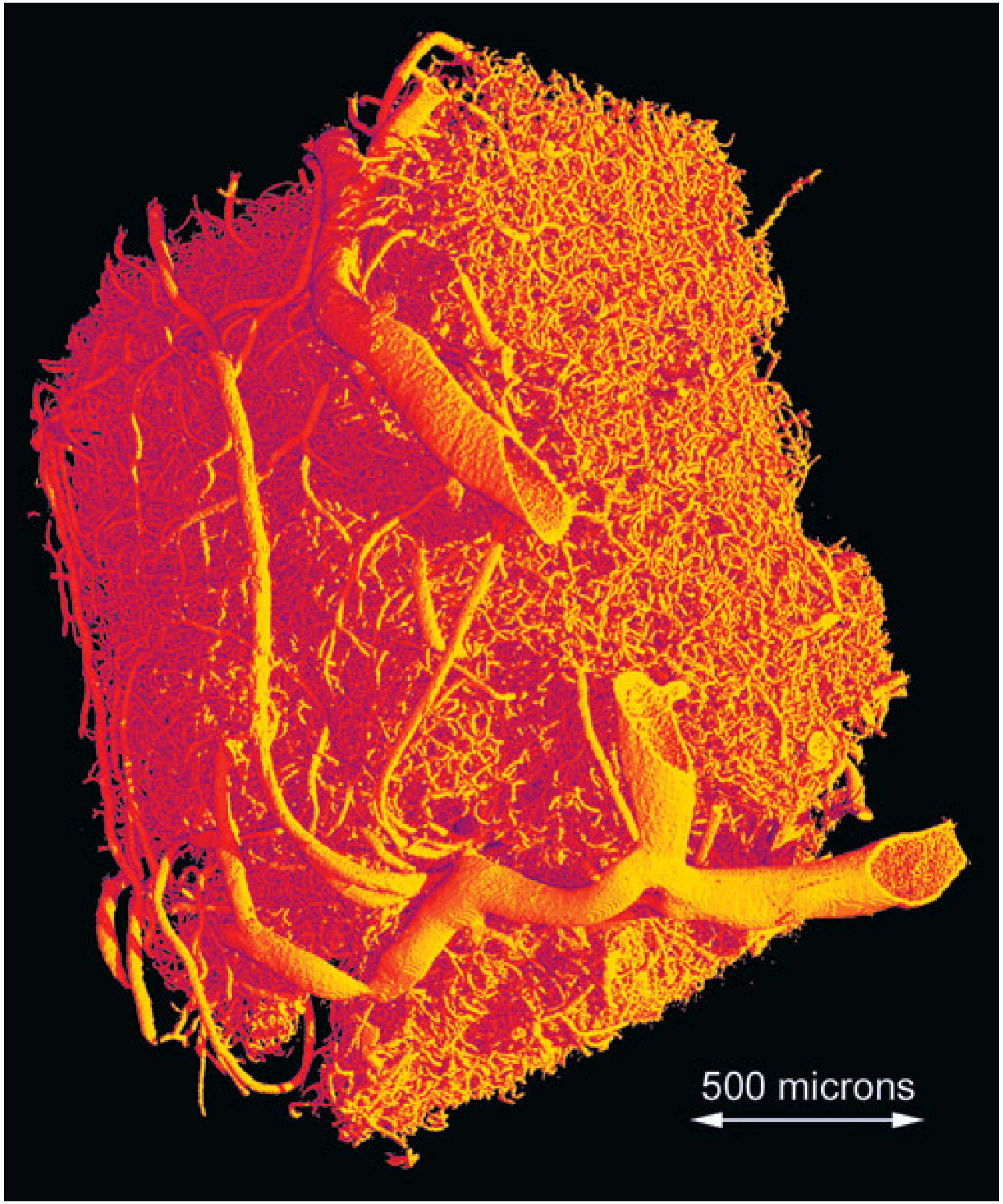

3-dim. reconstruction
of the brain of a rat

Swiss Light Source

The photoemission experiment

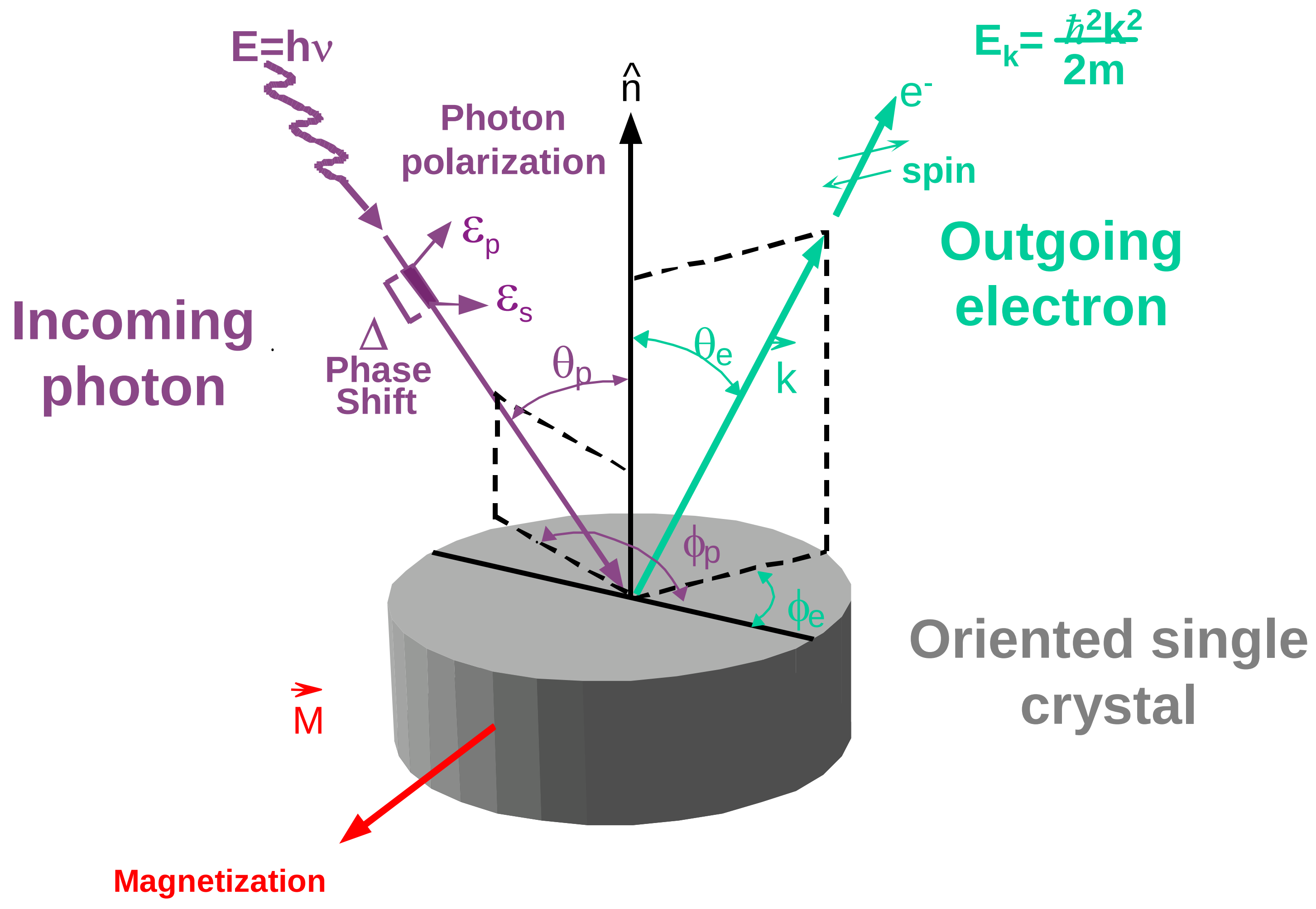

The electron must overcome the sample work function ϕ_{sample} in order to reach the vacuum; afterwards its energy is changed by the difference in work function between the analyzer and the sample. So:

$$E_k^{meas} = h\nu - E_b - \phi_{analyzer}$$

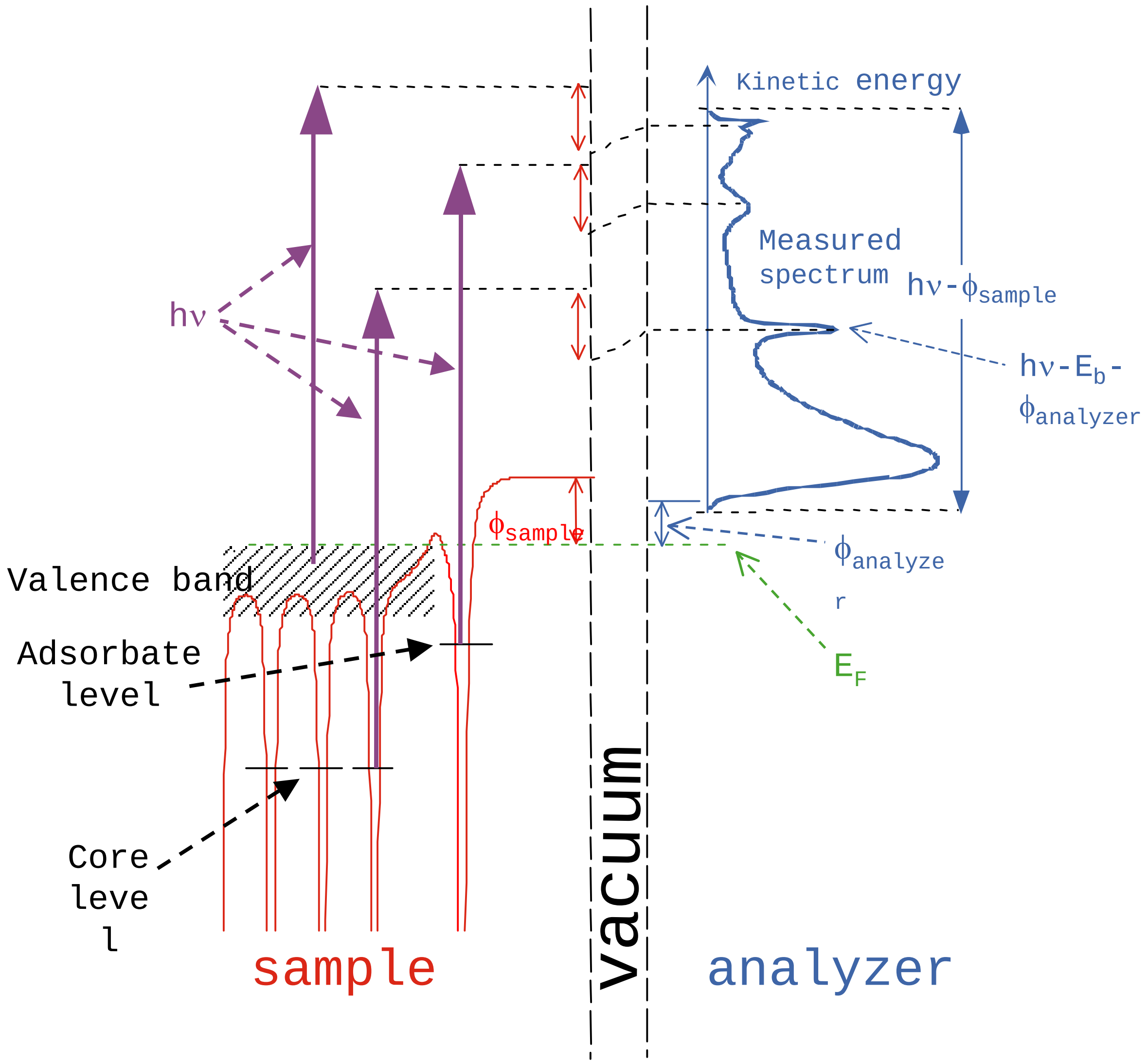

The SPELEEM

Spectroscopic photoemission and low energy electron microscope

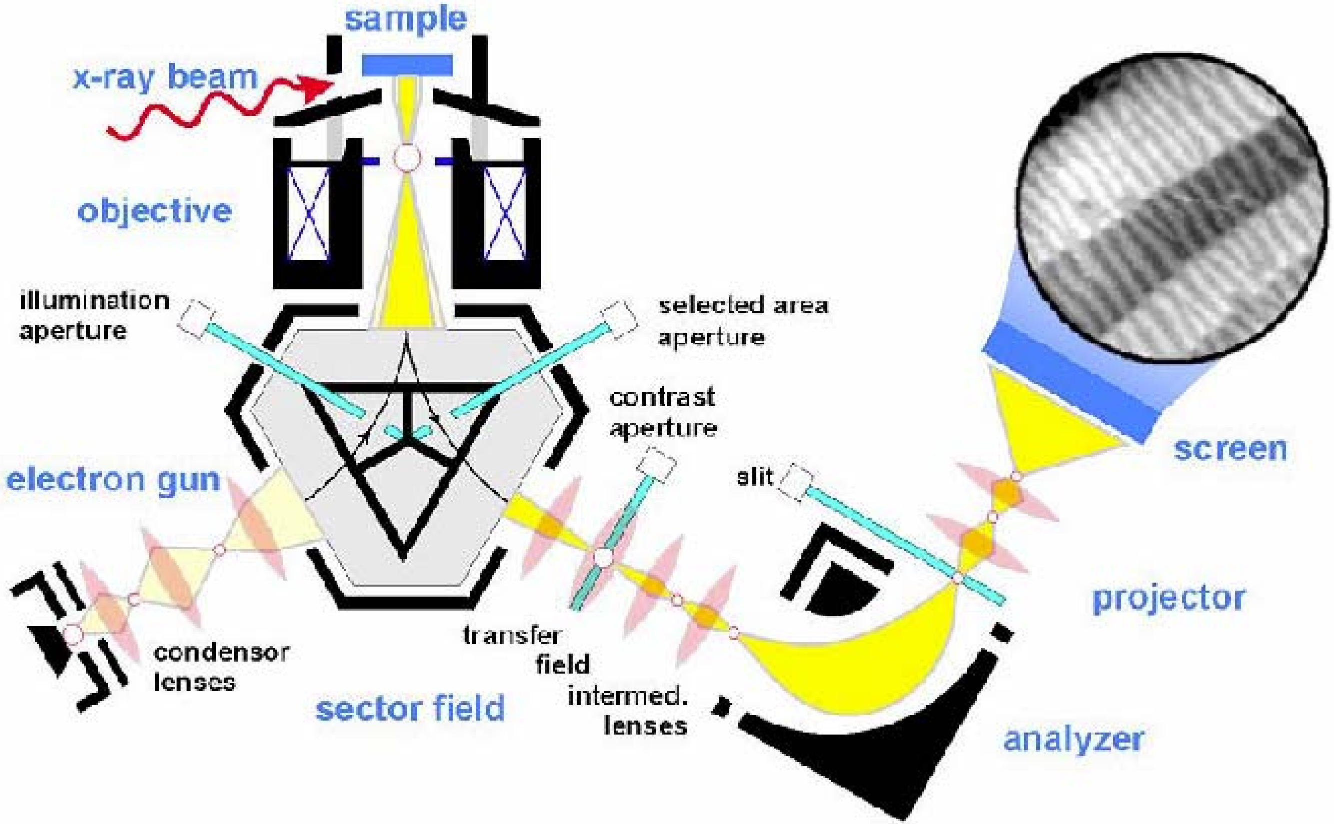

The SPELEEM at ELETTRA

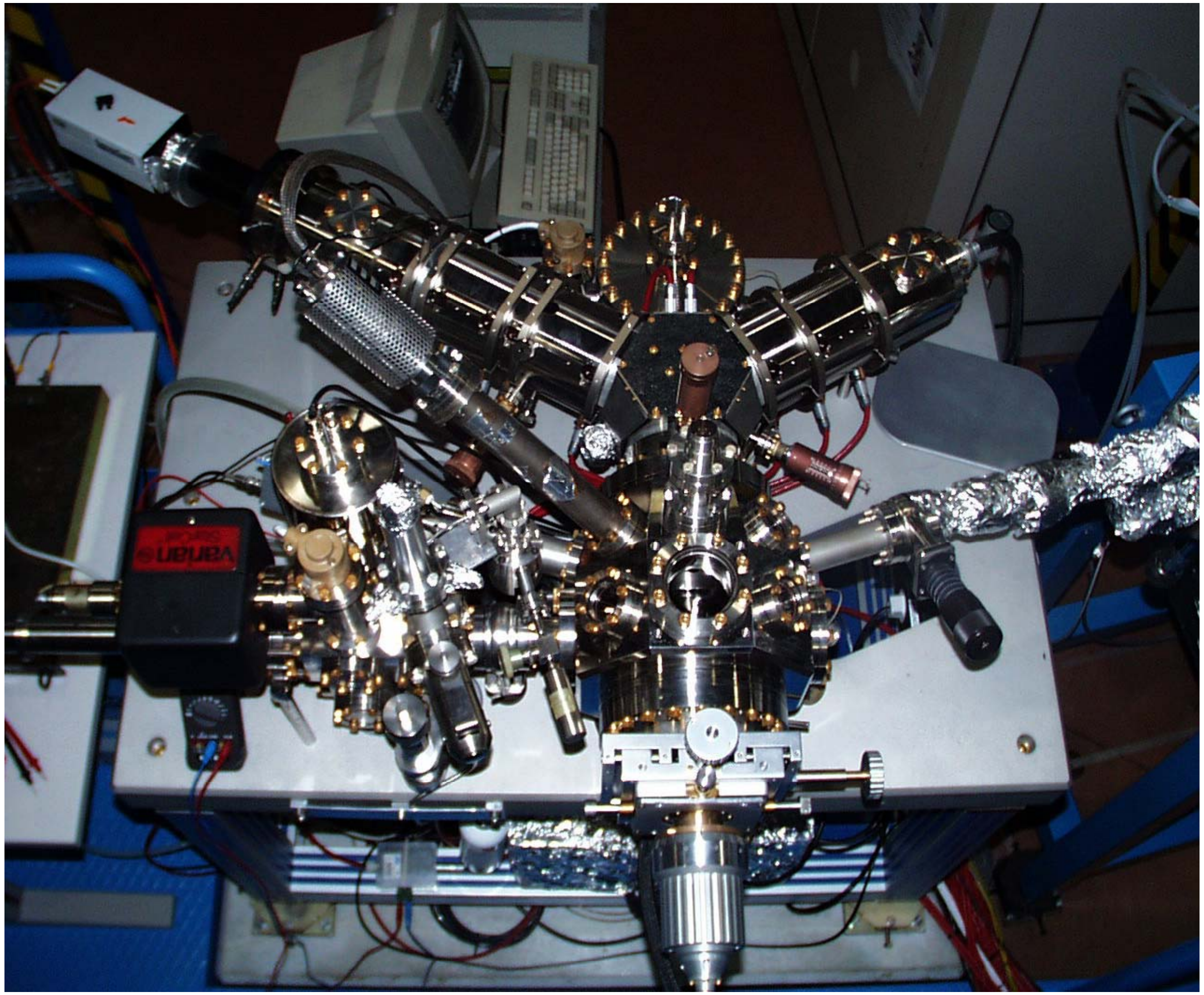

Nanospectroscopy Beamline

VOLUME 93, NUMBER 19 PHYSICAL REVIEW LETTERS week ending 5 NOVEMBER 2004

Tuning Surface Reactivity via Electron Quantum Confinement

L. Aballe,* A. Barinov,* A. Locatelli, S. Heun,† and M. Kiskinova*,‡

Sinctrotrone Trieste, Area Science Park, Basovizza 34012 Trieste, Italy

(Received 9 August 2004; published 4 November 2004)

The effect of electron quantum confinement on the surface reactivity of ultrathin metal films is explored by comparing the initial oxidation rate of atomically flat magnesium films of different thickness, using complementary microscopy techniques. Pronounced thickness-dependent variations in the oxidation rate are observed for well ordered films of up to 15 atomic layers. Quantitative comparison reveals direct correlation between the surface reactivity and the periodic changes in the density of electronic states induced by quantum-well states crossing the Fermi level.

DOI: 10.1103/PhysRevLett.93.196103 PACS numbers: 82.65.+r, 68.37.Nq, 68.37.Yz, 68.65.Fg

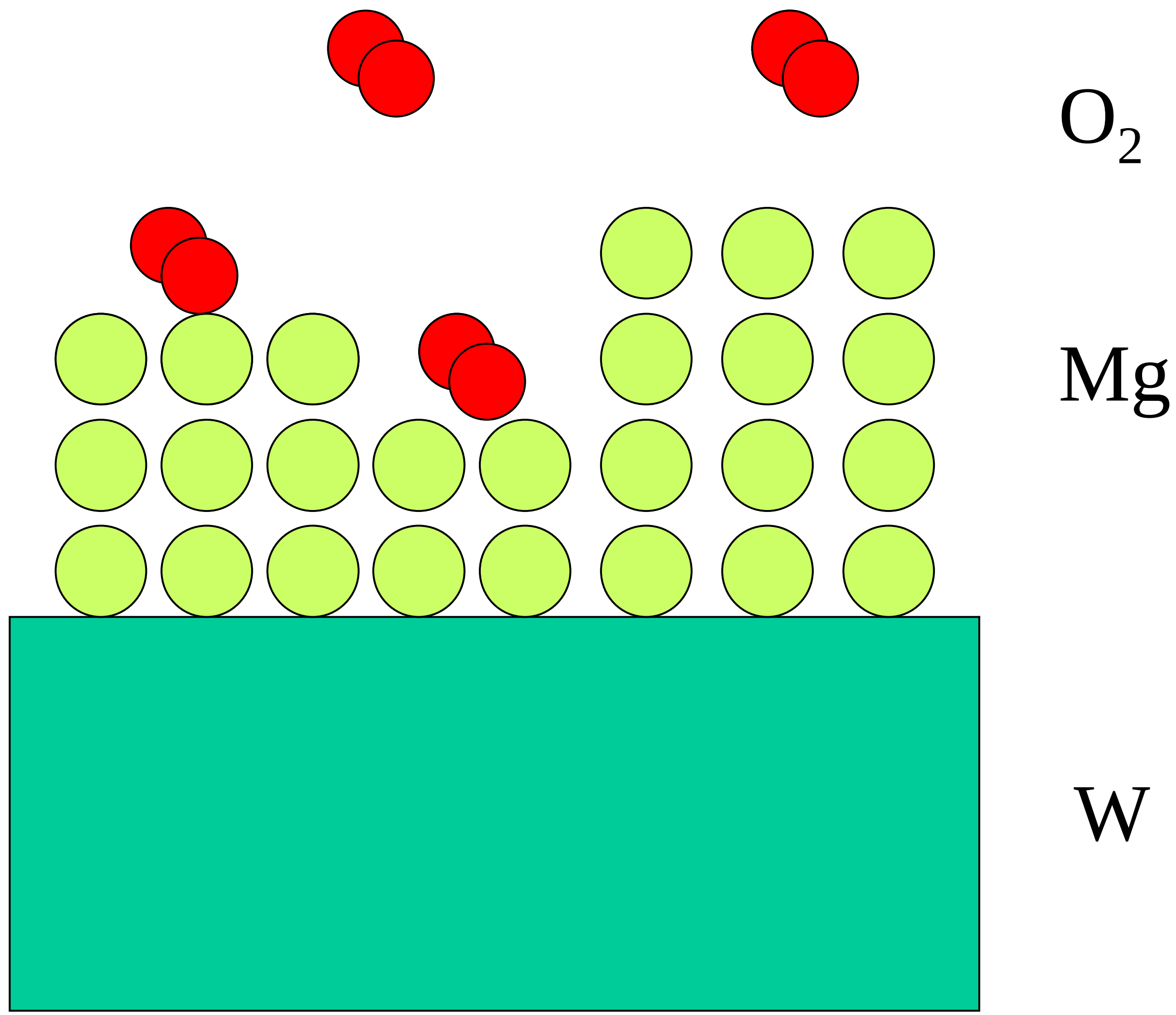

Mg layers on W substrate

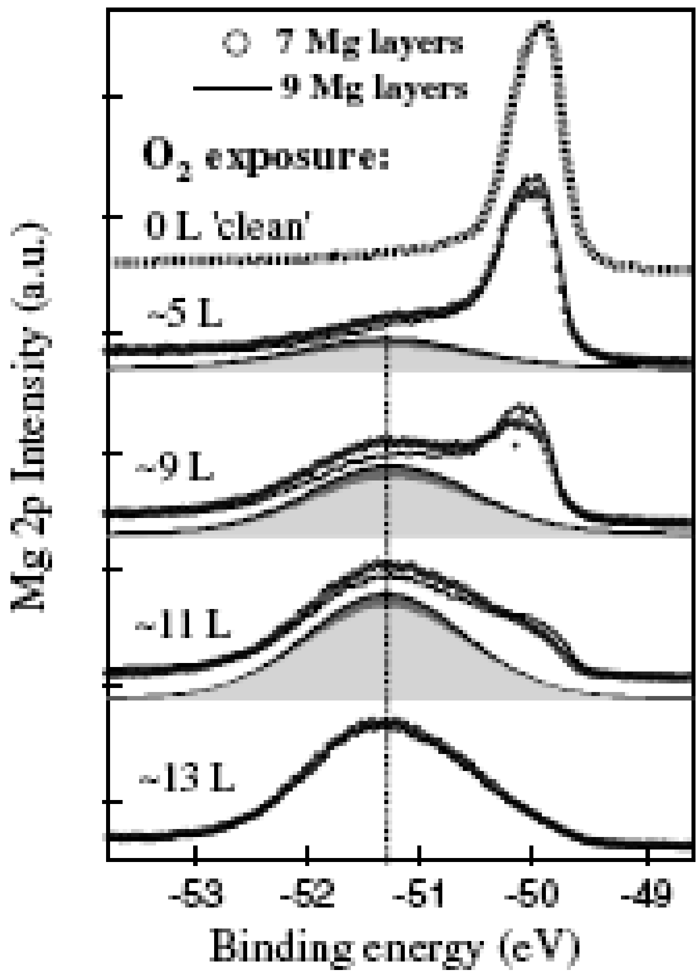

FIG. 3. The evolution of the Mg 2*p* spectra upon increasing the oxygen dose for films of seven and nine atomic layers. The broad component corresponds to the photoelectron emission from the Mg atoms bonded to oxygen.

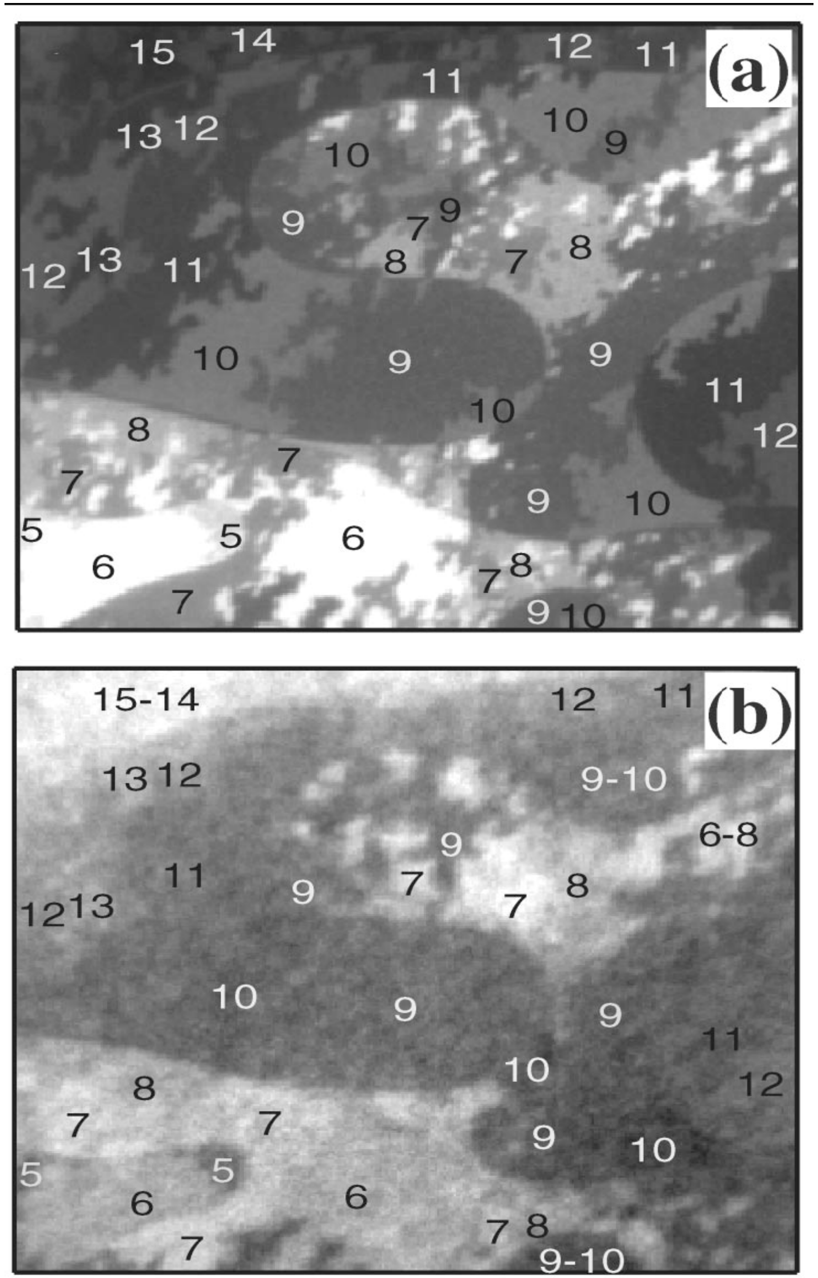

6.5 μm2 images of a Mg film in an advanced growth stage. (a) 1.3 eV LEEM image: the indicated number of atomic layers corresponding to the microregions was determined following the reflectivity changes [24] during the film growth at 120 C with deposition rate of 0.1 atomiclayer/min. (b) XPEEM image of the same Mg film after exposure to 9 L of O2 at 50 C, where the contrast corresponds to the extent of local Mg oxidation. The image is obtained by measuring the Mg 2p intensity of oxidized Mg, I_{ox} .

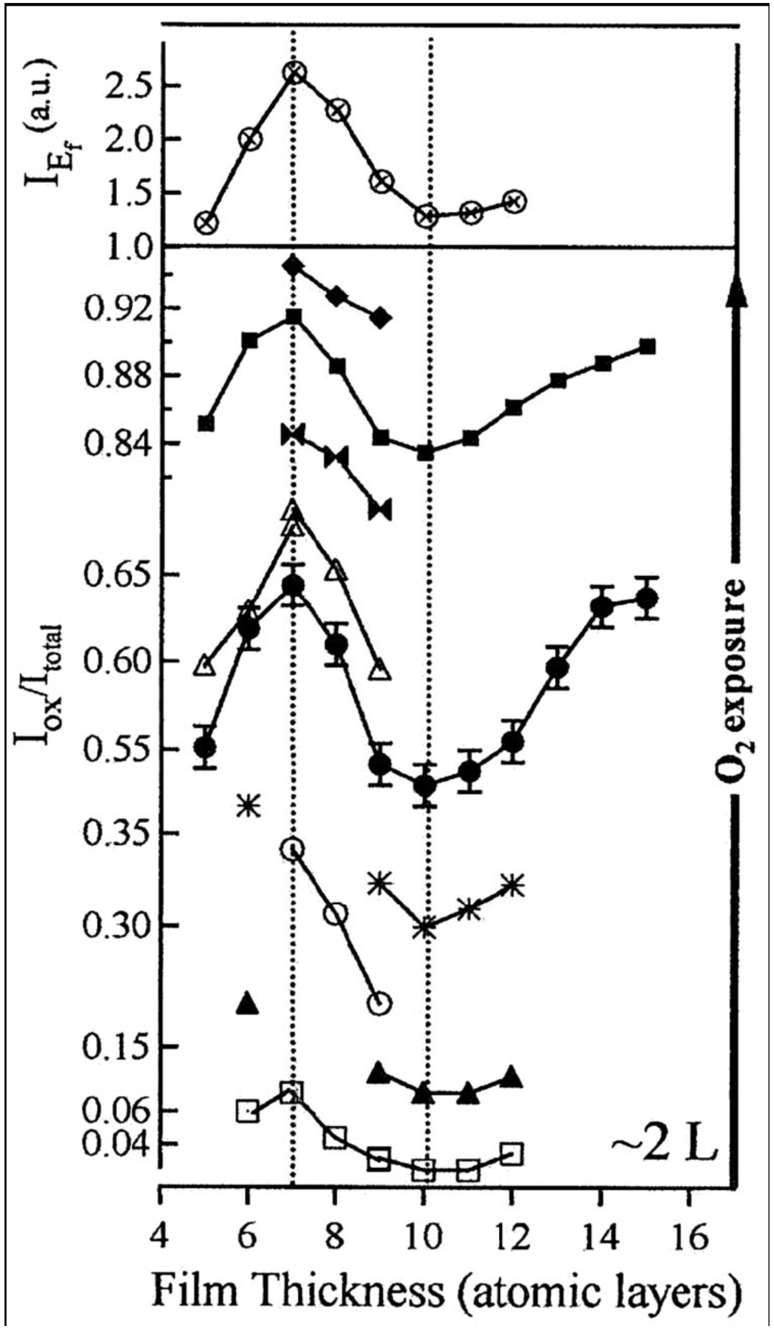

FIG. 4. (Lower panel) Plots of the relative weight of the Mg 2p oxide component, I_{ox}/I_{total}, obtained in several experimental runs. Data indicated with the same symbols correspond to the same O2 exposure. (Upper panel) Photoemission intensity at the Fermi level measured for different microregion thickness before oxygen exposure with energy resolution of 0.25 eV.

Spectromicroscopy Beamline

VOLUME 93, NUMBER 9 PHYSICAL REVIEW LETTERS week ending 27 AUGUST 2004

Direct Observation of Large Electronic Domains with Memory Effect in Doped Manganites

D. D. Sarma,* Dinesh Topwal, and U. Manju
Solid State and Structural Chemistry Unit, Indian Institute of Science, Bangalore, 560012, India

S. R. Krishnakumar
International Centre for Theoretical Physics (ICTP), Strada Costiera 11, 34100 Trieste, Italy

M. Bertolo, S. La Rosa, and G. Cautero
Sincrotrone Trieste, S.S. 14 km 163.5 - in AREA Science Park, 34012 Basovizza, Trieste, Italy

T. Y. Koo, P. A. Sharma, and S.-W. Cheong
Department of Physics and Astronomy, Rutgers University, New Jersey 08854, USA

A. Fujimori
Department of Complexity Science and Engineering, University of Tokyo, 5-1-5 Kashiwanoha, Kashiwa, Chiba 277-8561, Japan
(Received 11 June 2004; published 25 August 2004)

We use a spatially resolved, direct spectroscopic probe for electronic structure with an additional sensitivity to chemical compositions to investigate high-quality single crystal samples of $La_{1/4}Pr_{3/8}Ca_{3/8}MnO_3$, establishing the formation of distinct insulating domains embedded in the metallic host at low temperatures. These domains are found to be at least an order of magnitude larger in size compared to previous estimates and exhibit memory effects on temperature cycling in the absence of any perceptible chemical inhomogeneity, suggesting long-range strains as the probable origin.

Spectromicroscopy Beamline

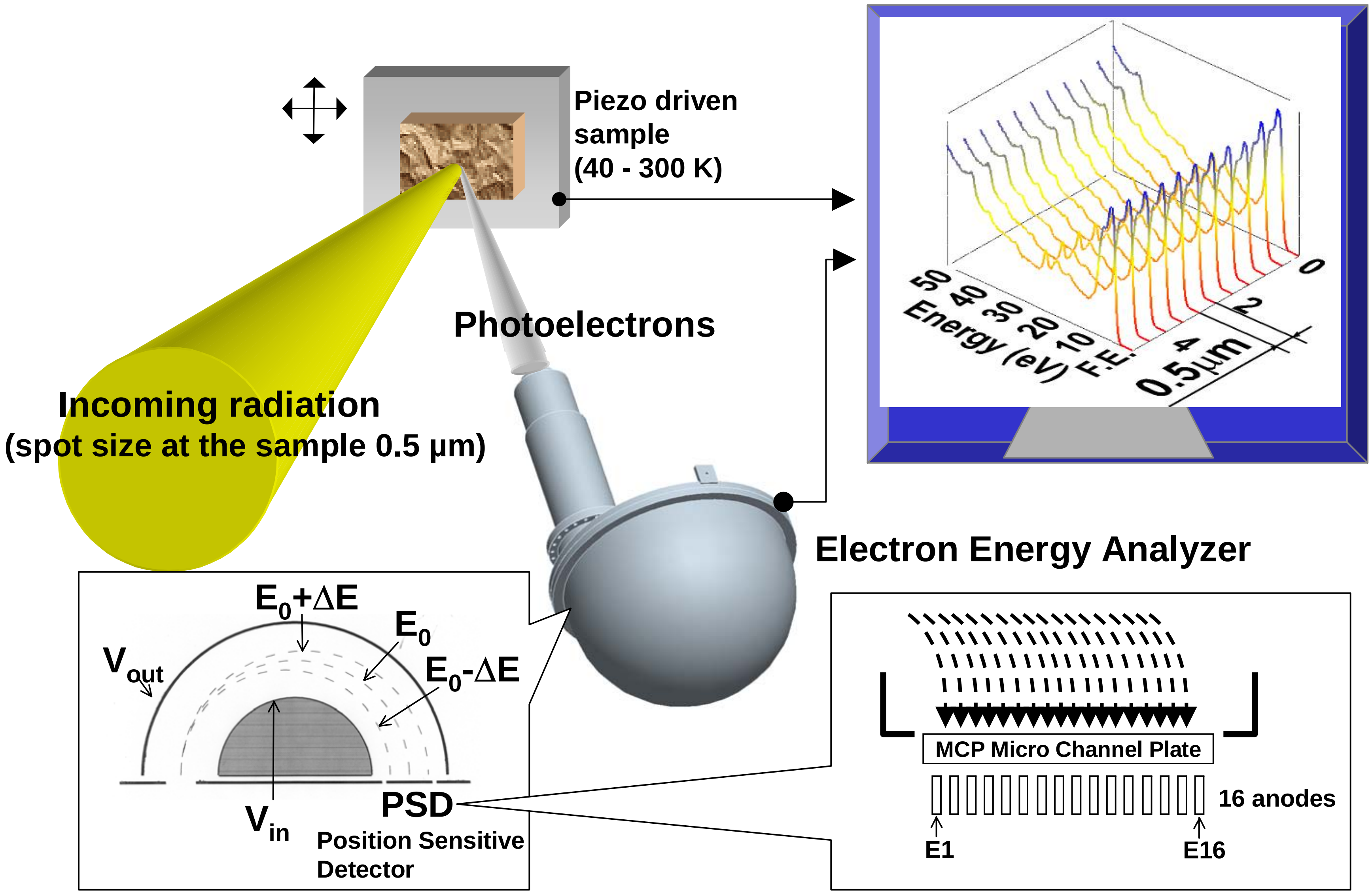

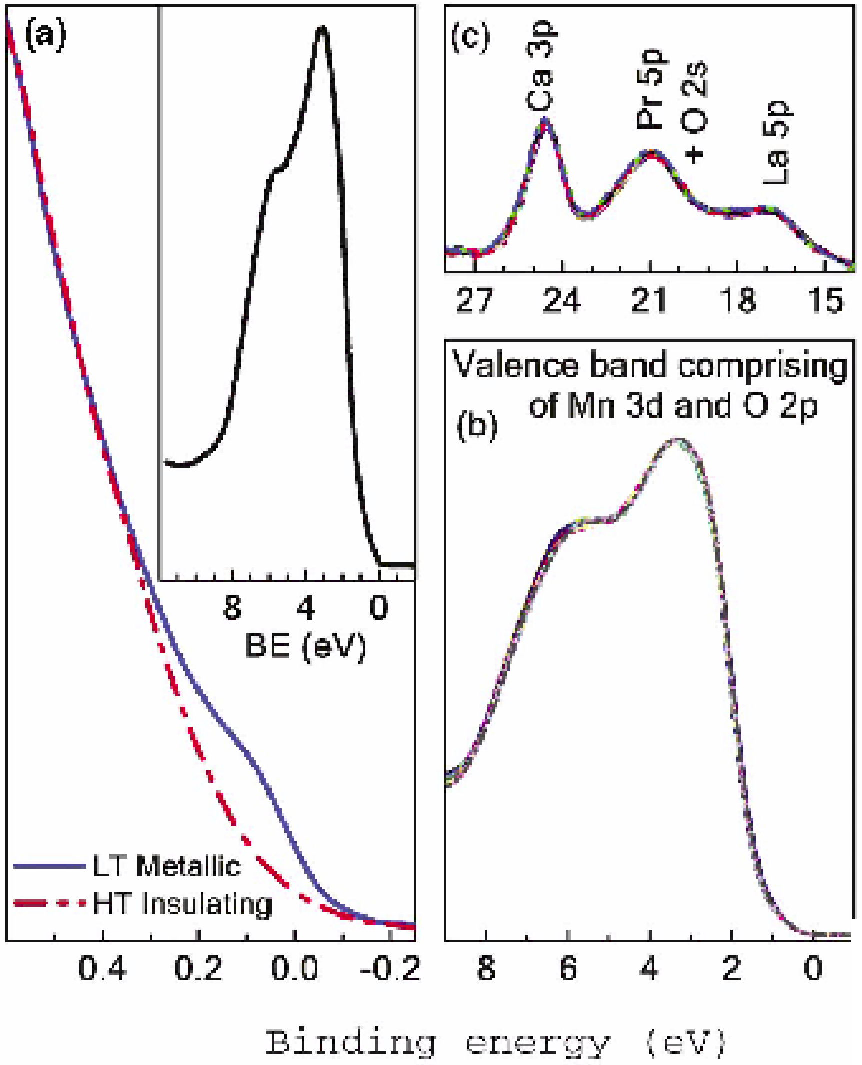

$La_{0.25}\ Pr_{0.375}\ Ca_{0.375}\ MnO_3$

FIG. 2 (color online). . (a) Spectral changes close to the Fermi energy across the metal-insulator transition, exhibiting a finite density of states at E_F in the metallic phase. The inset shows the overall spectral feature over a wide energy range. (b) Superposition of valence band spectra consisting of mainly Mn $3d$ and O $2p$ states recorded with a high spatial resolution (0.5 μm) at 28 different spots on the sample. (c) Superposition of the shallow core level spectra from La, Pr and Ca after a linear background subtraction from the same set of spots as in panel (b).

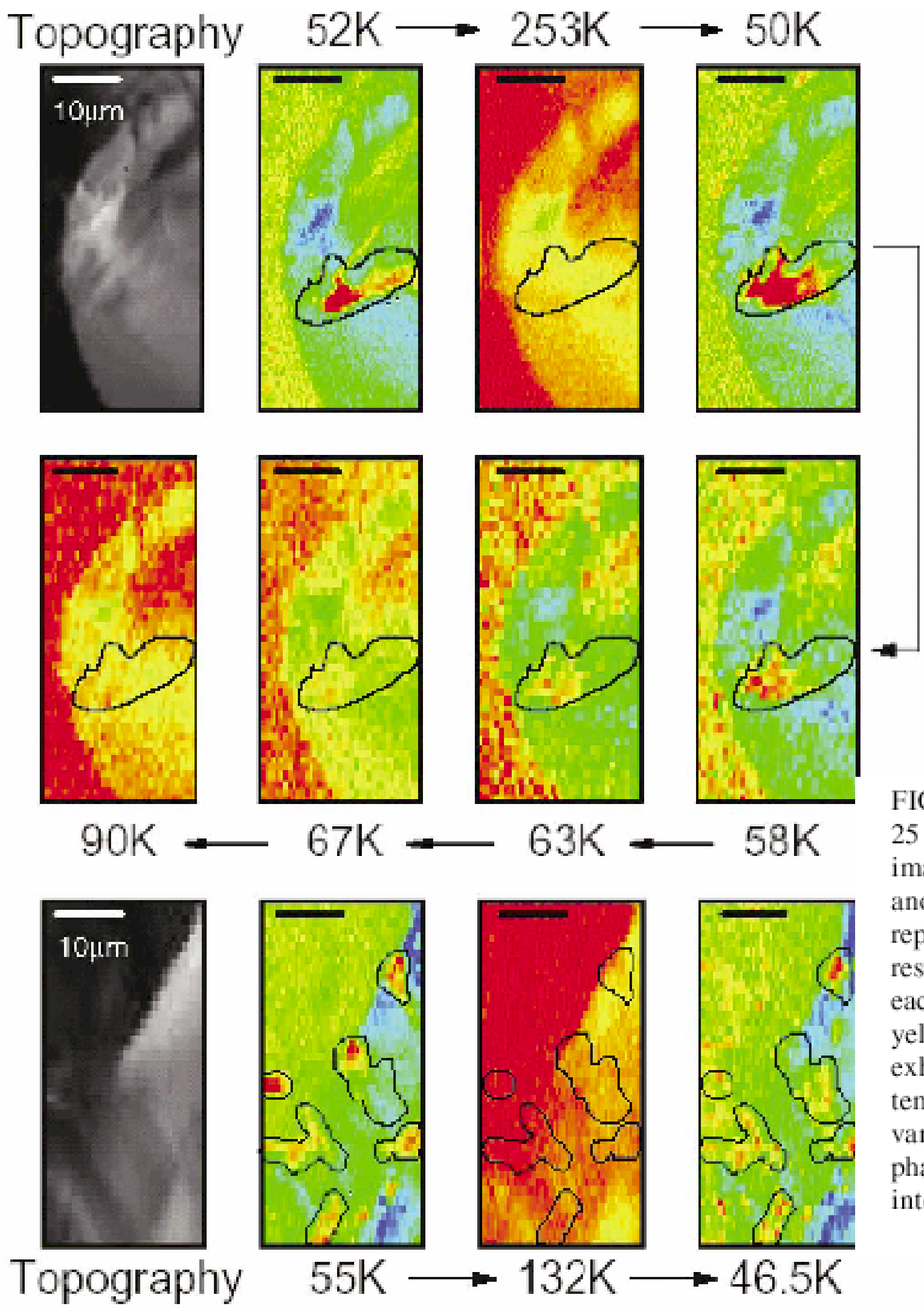

Red-yellow = insulator

Blue-green = metal

FIG. 3 (color). . Spectromicroscopic images over $\sim 54 \times 25\ \mu m^2$ areas of the sample surface. The top two rows show images from one region of the sample and the bottom row from another part, with the first panel in each of the two sets represented by gray scale being a topographic image and the rest ratio images. Ratio images at the lowest temperature for each image show emergence of distinct insulating patches (red-yellow) deep within the metallic regime (blue-green), which exhibit memory effects in the formation and morphology on temperature cycling. The color contrast in the ratio images vanishes and the entire sample transforms into the insulating phase as the temperature is increased, converting the system into an electronically homogeneous phase.

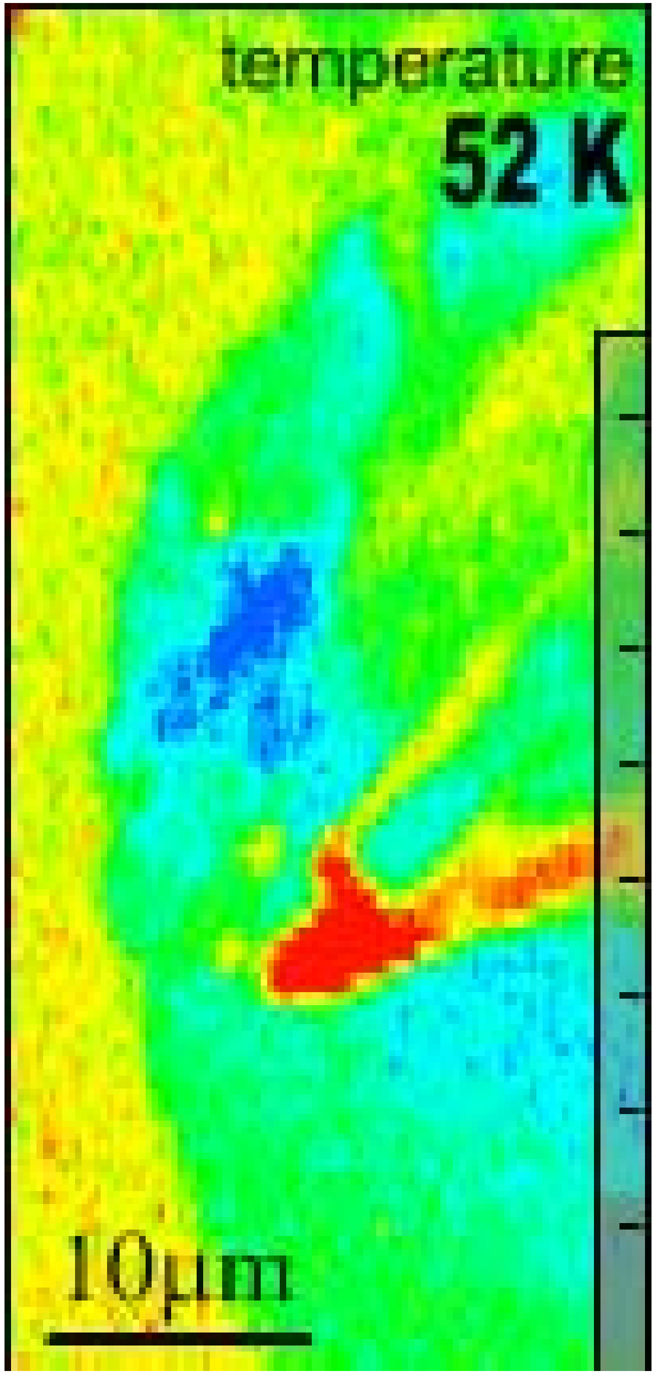

temperature
52 K
10μm

elettra

X-Ray Diffraction Beamline

Coronavirus Main Proteinase ($3CL^{pro}$) Structure: Basis for Design of Anti-SARS Drugs

Kanchan Anand,[1,2]† John Ziebuhr,[3]† Parvesh Wadhwani,[4] Jeroen R. Mesters,[1,2] Rolf Hilgenfeld[1,2]*

A novel coronavirus has been identified as the causative agent of severe acute respiratory syndrome (SARS). The viral main proteinase (M^{pro}, also called $3CL^{pro}$), which controls the activities of the coronavirus replication complex, is an attractive target for therapy. We determined crystal structures for human coronavirus (strain 229E) M^{pro} and for an inhibitor complex of porcine coronavirus [transmissible gastroenteritis virus (TGEV)] M^{pro}, and we constructed a homology model for SARS coronavirus (SARS-CoV) M^{pro}. The structures reveal a remarkable degree of conservation of the substrate-binding sites, which is further supported by recombinant SARS-CoV M^{pro}-mediated cleavage of a TGEV M^{pro} substrate. Molecular modeling suggests that available rhinovirus $3C^{pro}$ inhibitors may be modified to make them useful for treating SARS.

***Science*, 300, 1763 (2003)**

Protein Crystallography at Elettra

Fig. 2. Dimer of HCoV M^{pro}. The N-terminal residues of each chain squeeze between domains II and III of the parent monomer and domain II of the other monomer. N and C termini are labeled by cyan and magenta spheres and the letters N and C, respectively.

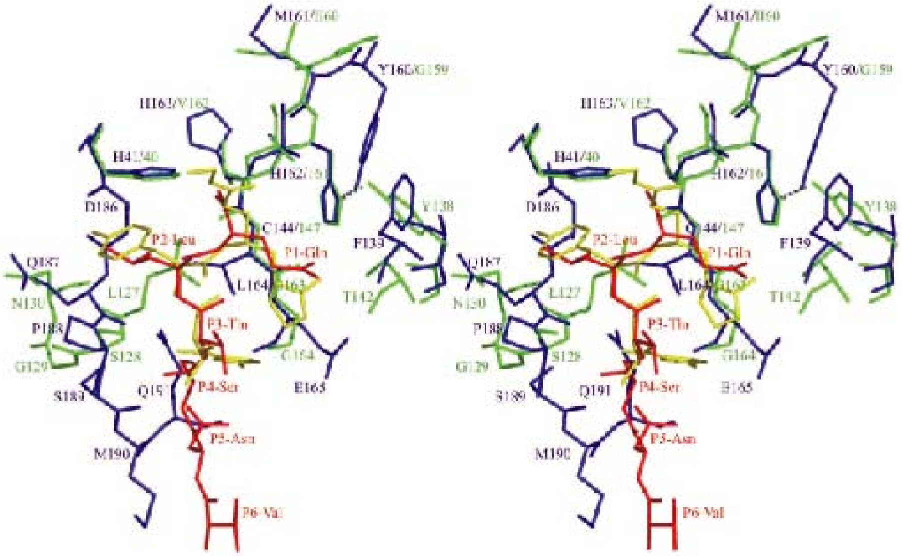

Fig. 4. Derivatives of the antirhinoviral drug AG7088 should inhibit coronavirus M^{pro}s. A superimposition (stereo image) of the substrate-binding regions of TGEV M^{pro} (marine) in complex with the hexapeptidyl CMK inhibitor (red) and HRV2 3C^{pro} (green) in complex with the inhibitor AG7088 (yellow) is shown.

Structure of a gametocyte protein essential for sexual development in *Plasmodium falciparum*

Amit Sharma[1], Indu Sharma[1], Darin Kogkasuriyachai[2] and Nirbhay Kumar[2]

Published online 10 February 2003; doi:10.1038/nsb899

Malaria transmission is dependent on the development of sexual forms of *Plasmodium falciparum*, called gametocytes, in the vertebrate host. Pfg27 is an abundantly expressed sexual stage–specific protein that is essential for gametocytogenesis in *P. falciparum*. We describe the crystal structure of Pfg27, which reveals a novel fold composed of two pseudo dyad–related repeats of the helix-turn-helix motif. Structurally equivalent helices of each repeat either form a dimer interface or interact with RNA *in vitro*. One side of the dimer presents an unprecedented juxtaposition of four polyproline (PXXP) motifs. Preliminary binding data indicate that these sites are capable of binding Src homology-3 (SH3) modules. Molecular modeling suggests that the dimer can accommodate two SH3 modules simultaneously, potentially enabling molecular crosstalk between SH3-containing proteins. The structural and initial biochemical evidence suggests that Pfg27 may serve as a platform for RNA and SH3 binding.

nature structural biology • volume 10 number 3 • march 2003

Nature Struct. Biol. **10**, 197 (2003)

Clean Room of the Elettra/INFM/CNR "LILIT" beamline

ELETTRA: Strong efforts in nanofabrication

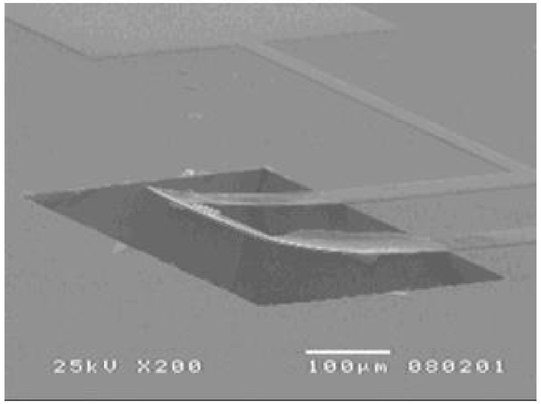

Cantilever for gas sensors

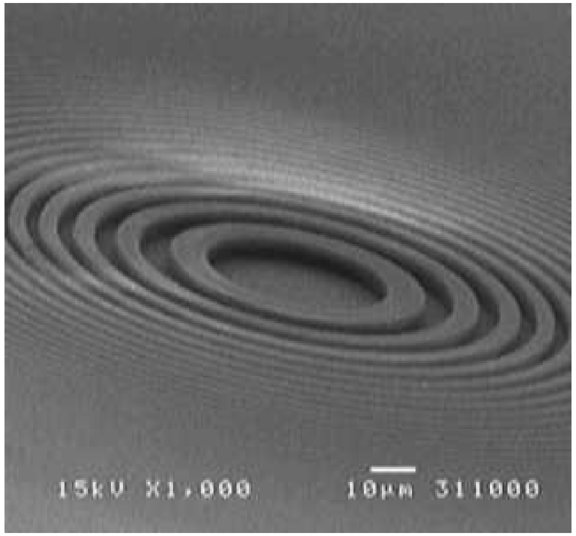

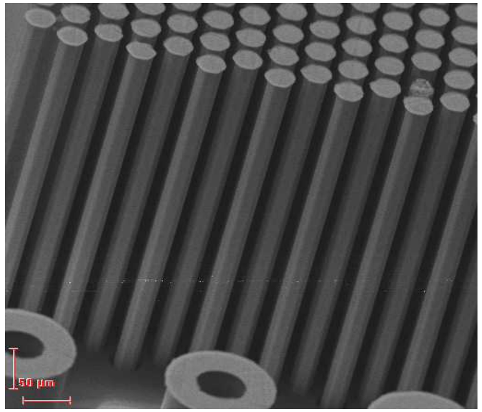

DeepX-ray lithography

X-ray optics

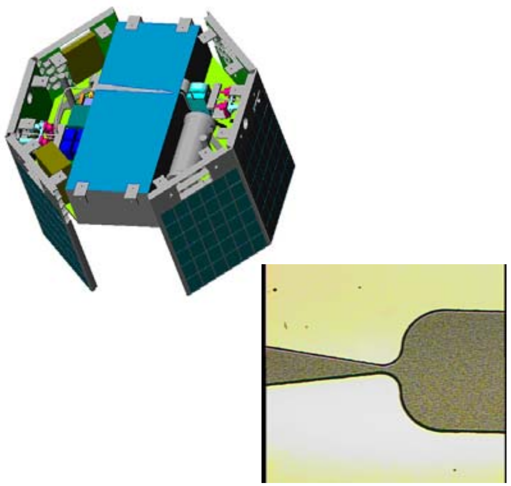

Micro-propulsion systems for microsatellite's control and correction

3D photonic crystals

Di Fabrizio et al., TASC-INFM

ELETTRA: Strong efforts in nanofabrication

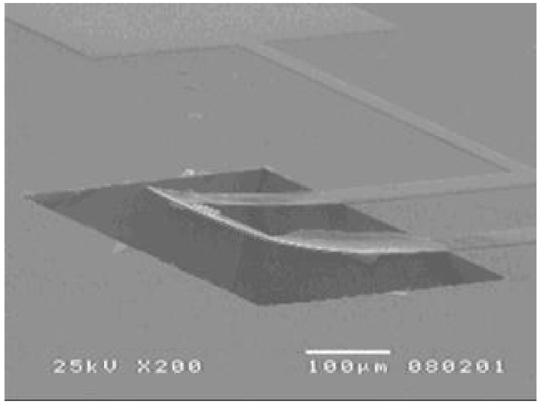

Cantilever for gas sensors

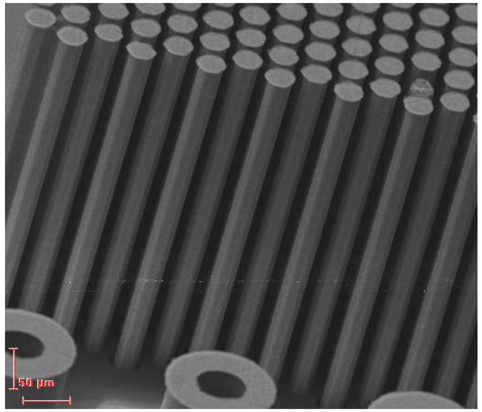

DeepX-ray lithography

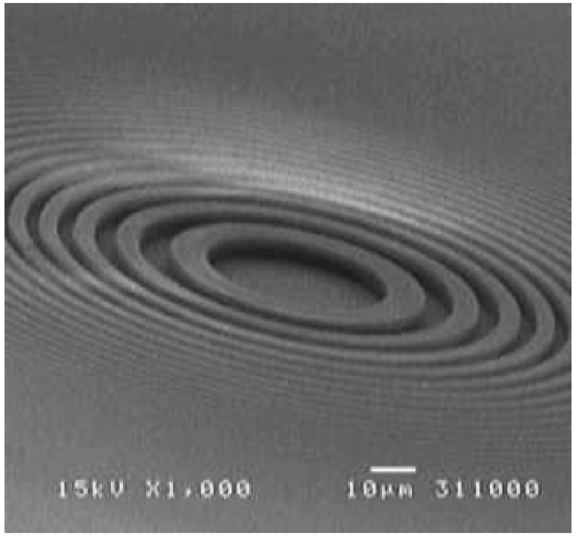

X-ray optics

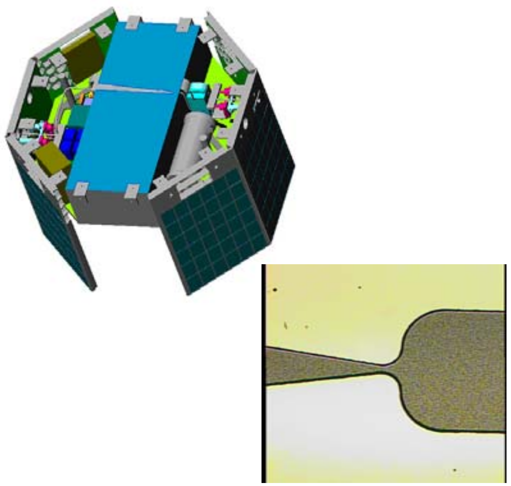

Micro-propulsion systems for microsatellite's control and correction

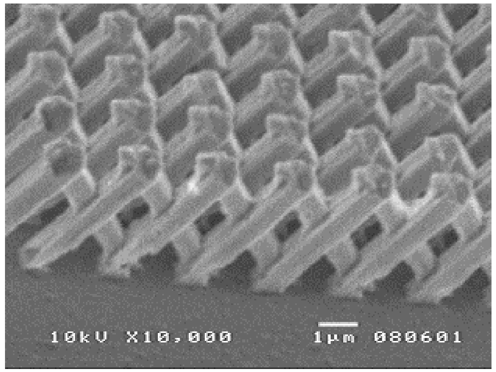

3D photonic crystals

Di Fabrizio et al., TASC-INFM

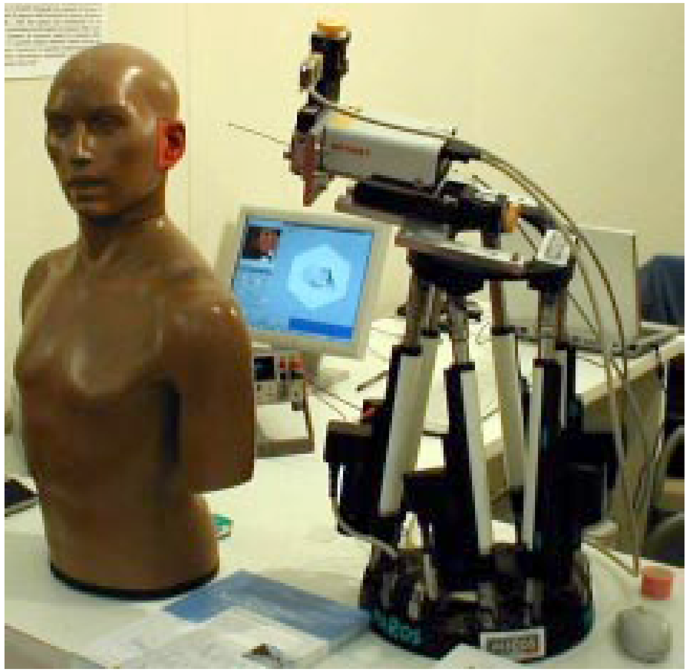

First prototype of human ear scanning optical system.

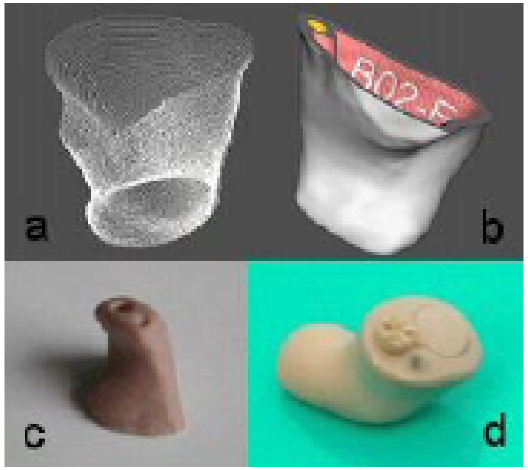

Data Point Cloud Image, STL Format Surface, Fabricated Mold from STL File, Final Hearing-aid

THE CASE

We used the conoscopic interferometry setup and data acquisition with a new design of scanning probe based on the torsional micromirror actuated with electromagnetic force. Electromagnetic actuation was achieved by controlling the current in copper coil of electromagnet. The mirror directs the incident laser light to the ear surface then, having the tilt angle of the mirror, we can obtain a line-scan of the sample.

Our MEMS micromirror consists of 2 parts: a structural support plate made of electroplated copper on which a free standing mirror is resting. This structural plate takes back the mirror on the initial position when the induction field is removed.

In order to fabricate the hearing aid from the point cloud, the ear canal is defined by a mesh of tiny triangles laid over the surfaces (STL format). STL is a standard output format from most CAD (computer-aided design) software and the standard file format for the rapid prototyping.

International Patented Pending n. PCT/IT03/00366 Inventors: E. DI FABRIZIO, S. CABRINI, A. D. COJOC

THE CASE

Sincrotrone Trieste S.C.p.A. and INFM-TASC, in collaboration with Mechatronic GmbH (project leader), have developed a **microturbine** to be used as electrical generator in a liquid bipropellant **micro-rocket engine for micro/nanosatellites***.

The turbine microrotors are fabricated with LIGA technology (Litografie = Lithography, Galvanoformung = Electrodeposition, Abformung = Molding) and EDM (Electro Discharge Machining). In fact, LIGA is well suited for the production of high aspect ratio microstructures with very steep and well polished side walls. Moreover, it does not limit the choice of materials to silicon and derivative materials but, coupled with EDM, offers the possibility to fabricate turbines made of metallic compounds or any electrically conductive material.

**Project funded by ESA.*
Contract number 16914/02/NL/SFe

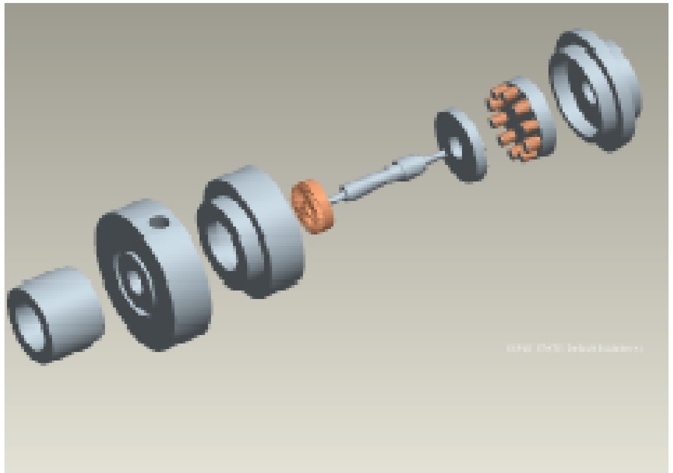

Exploded view of a microturbine assembled in the generator system.

Copper electrode, stainless steel (left) and aluminum (right) microrotors of 10 mm diameter.

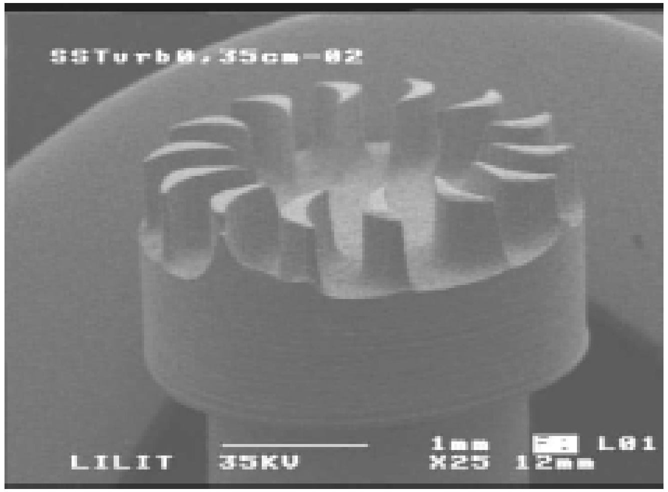

SEM image of a stainless steel rotor of 3.2 mm diameter.